

## Article

# Ore Genesis of the Changkeng–Fuwan Au–Ag Deposit in Central Guangdong, South China: Evidence from Fluid Inclusions and C–H–O–S–Pb–He–Ar Isotopes

Guangyao Shi <sup>1,2</sup>, Jianling Xue <sup>3,\*</sup>, Xiaoqiang Zhu <sup>4,\*</sup>, Zhenshan Pang <sup>3</sup>, Xueqiu Wang <sup>1</sup>, Fan Yang <sup>5</sup> , Gilby Jepson <sup>6</sup>, Wen Tao <sup>3</sup> and Shimin Zhen <sup>3</sup>

- <sup>1</sup> Institute of Geophysical and Geochemical Exploration, Chinese Academy of Geological Sciences, Langfang 065000, China; sguangyao0001@163.com (G.S.); wxueqiu@mail.cgs.gov.cn (X.W.)  
<sup>2</sup> School of Earth Sciences and Resources, China University of Geosciences Beijing, Beijing 100083, China  
<sup>3</sup> Development and Research Center, China Geology Survey, Beijing 100037, China; pzs927@163.com (Z.P.); taowendj@163.com (W.T.); zhenshmin0001@163.com (S.Z.)  
<sup>4</sup> School of Geography and Tourism, Anhui Normal University, Wuhu 241000, China  
<sup>5</sup> Key Laboratory of Mineral Resources in Western China (Gansu Province), School of Earth Sciences, Lanzhou University, Lanzhou 730000, China; fanyang@lzu.edu.cn  
<sup>6</sup> Department of Geosciences, University of Arizona, Tucson, AZ 85721, USA; gjepson@arizona.edu  
\* Correspondence: xuejianling369@126.com (J.X.); zhuxq@ahnu.edu.cn (X.Z.)



**Citation:** Shi, G.; Xue, J.; Zhu, X.; Pang, Z.; Wang, X.; Yang, F.; Jepson, G.; Tao, W.; Zhen, S. Ore Genesis of the Changkeng–Fuwan Au–Ag Deposit in Central Guangdong, South China: Evidence from Fluid Inclusions and C–H–O–S–Pb–He–Ar Isotopes. *Minerals* **2022**, *12*, 799.

<https://doi.org/10.3390/min12070799>

Academic Editors: Jan Marten Huizenga, Kunfeng Qiu and Callum Hetherington

Received: 2 April 2022  
Accepted: 20 June 2022  
Published: 23 June 2022

**Publisher's Note:** MDPI stays neutral with regard to jurisdictional claims in published maps and institutional affiliations.



**Copyright:** © 2022 by the authors. Licensee MDPI, Basel, Switzerland. This article is an open access article distributed under the terms and conditions of the Creative Commons Attribution (CC BY) license (<https://creativecommons.org/licenses/by/4.0/>).

**Abstract:** The Changkeng–Fuwan Au–Ag deposit is representative in South China, which is located in the southwest of the Qin–Hang metallogenic belt (QHMB). The Au and Ag orebodies are located in the same altered fracture zone, forming independent gold and silver orebodies respectively, with the characteristics of “upper gold and lower silver” in space. Three metallogenic stages have been identified: the pyrite–quartz–sericite stage, the polymetallic sulfide stage, and the quartz–calcite stage. The fluid inclusions (FIs) from the deposit are the two-phase liquid-rich (type I) and the pure liquid FIs (type II). The microthermometric measurements of type I FIs are characterized by temperatures of 158–282 °C and 146–289 °C and salinities of 0.35–9.88 wt.% NaCl equiv. and 0.18–11.70 wt.% NaCl equiv. The H, O, He, and Ar isotopic data show that the ore-forming fluids of the deposit were derived from a mixture of magmatic and meteoric fluids. The C and O isotopic data suggest that the carbon of the fluid may derive from a magmatic source. The S and Pb isotopic data indicate that the primary source of the metals in the Changkeng–Fuwan deposit may be a magma source. Based on the geological characteristics, FI microthermometry, and isotope data (C, H, O, He, Ar, S, and Pb), we propose that the Changkeng–Fuwan deposit should be classified as a far-source low-temperature magmatic–hydrothermal deposit.

**Keywords:** fluid inclusion; C–H–O–S–Pb–He–Ar isotopes; hydrothermal mineralization; Changkeng–Fuwan Au–Ag deposit; south China

## 1. Introduction

The Qin–Hang metallogenic belt (QHMB) is a 2000 km NE-trending ore belt situated in the South China Block [1–9]. The West Guangdong–East Guangxi, situated within the southwest of the QHMB, is one of the most important Cu–Au–Zn–Ag production areas in South China [10]. Numerous exploration studies have been conducted in the area during the past decades, resulting in the discovery of many large deposits [7,8,11,12], including the Pangxidong Ag deposit, the Damingshan Au–Ag deposit, the Hetai Au deposit, the Huangnikeng Au deposit, the Xinzhou Au deposit, and the Changkeng–Fuwan Au–Ag deposit.

The Changkeng–Fuwan Au–Ag deposit is one of the largest Au–Ag deposits in South China. The Au and Ag reserves reach large and super-large scales, respectively [13]. The Au and Ag orebodies are characterized by “upper gold and lower silver” in space. The

Changkeng–Fuwan Au–Ag deposit has been studied continuously since it was discovered in 1990 because of its special mineralization zonation. At present, its metallogenic process remains controversial. There are two views to interpret its metallogenic process: (1) the gold and silver mineralization were formed in different periods and different metallogenesis [14,15]; (2) the gold and silver mineralizations were formed in the same metallogenic system [16,17]. To address this problem, much research has been carried out on the Changkeng–Fuwan Au–Ag deposit. Previous studies on the Changkeng–Fuwan Au–Ag deposit have focused on the geology [15,18], the evolution of the ore-forming fluids [13,16,19,20], the source of the ore-forming metal [15,21,22], and the metallogenic epoch [13,23,24]. However, the origin of the ore-forming fluids and metal and the age of the deposit are still controversial. Du et al. [13] carried out K–Ar dating on the fluid inclusions in the quartz in the Changkeng–Fuwan Au–Ag deposit, which yielded ages of  $132 \pm 2.5$  and  $136.8 \pm 11.3$  Ma. Mao et al. [24] reported the quartz Rb–Sr isochron ages of  $128 \pm 3$  Ma and  $65 \pm 8.5$  in the Changkeng–Fuwan Au–Ag deposit, respectively. As to the origin of the ore-forming fluids, it has been proposed that the ore-forming fluids of the Changkeng–Fuwan Au–Ag deposit were derived from (1) meteoric water or formation water [15], (2) predominantly sedimentary brines [19], or (3) predominantly magmatic water [17]. Mao et al. [18] and Liang et al. [15] proposed that the ore-forming fluid of the Au mineralization was sourced from meteoric sources, whereas the ore-forming fluid of the Ag mineralization derived from a mixture of meteoric and magmatic sources. As to the source of the ore-forming materials, Sun et al. [25] and Zhang et al. [16] proposed that the Au and Ag were derived from the Zimenqiao Group host rock. However, Mao et al. [24] and Liang et al. [15] suggested that the Au was derived from the Zimenqiao Group host rock, and a potential source of Ag was from older basement rocks at depth.

In this study, we conducted detailed fieldwork, petrographic observations, fluid inclusions (FIs), and isotopic studies (C, H, O, He, Ar, S, and Pb) on the Au and Ag orebodies, respectively. The goals were to: (1) reveal the origin of the ore-forming fluids and metals as well as the ore deposition mechanism; (2) understand the ore genesis and mineralization zonation, (3) gain some insights into future exploration in the southwestern QHMB and SCB, and (4) provide an example for studying this type of deposit abroad.

## 2. Regional Geology

The South China Block consists of the Yangtze Block in the northwest and the Cathaysia Block in the southeast [26–29] (Figure 1a). The QHMB is located along the Neoproterozoic suture between the Yangtze and Cathaysian blocks and serves as the boundary along which the Neoproterozoic amalgamation took place. The belt is 2000 km long and 100–150 km wide, extending from Qinzhou Bay in eastern Guangxi Province, through northwestern Guangdong, southeastern Hunan, and central Jiangxi provinces, and then to Hangzhou Bay in Zhejiang Province [1,2]. The QHMB is a key metallogenic belt in South China, which hosts many economic deposits [7,8,30–34]. It has undergone multiple tectonic events associated with mineralization. As a result, the region is an important location for hydrothermal polymetallic mineralization [35–39]. Zhou et al. [4] divided the QHMB into three sections (Figure 1a). The southern section of the QHMB comprises the Yunkai Terrane and the Dayaoshan Uplift, which is an important gold producer in China [4,6–8] (Figure 1b). The Changkeng–Fuwan Au–Ag deposit is distributed in the northeast of the Yunkai Terrane. The lithostratigraphic units comprise a metamorphic basement and a sedimentary cover [9,40–42]. The main tectonic framework in the QHMB includes NE-trending faults and folds, which traverse the southern section [7,8,42–46]. Several ore deposits are distributed along these faults, but large deposits are hosted in the north segment such as the Hetai Au deposit and the Changkeng–Fuwan Au–Ag deposit (Figure 1b). Numerous Early Paleozoic and Mesozoic granitoids are exposed in the northwest of the Yunkai Terrane [40,43,47–49].

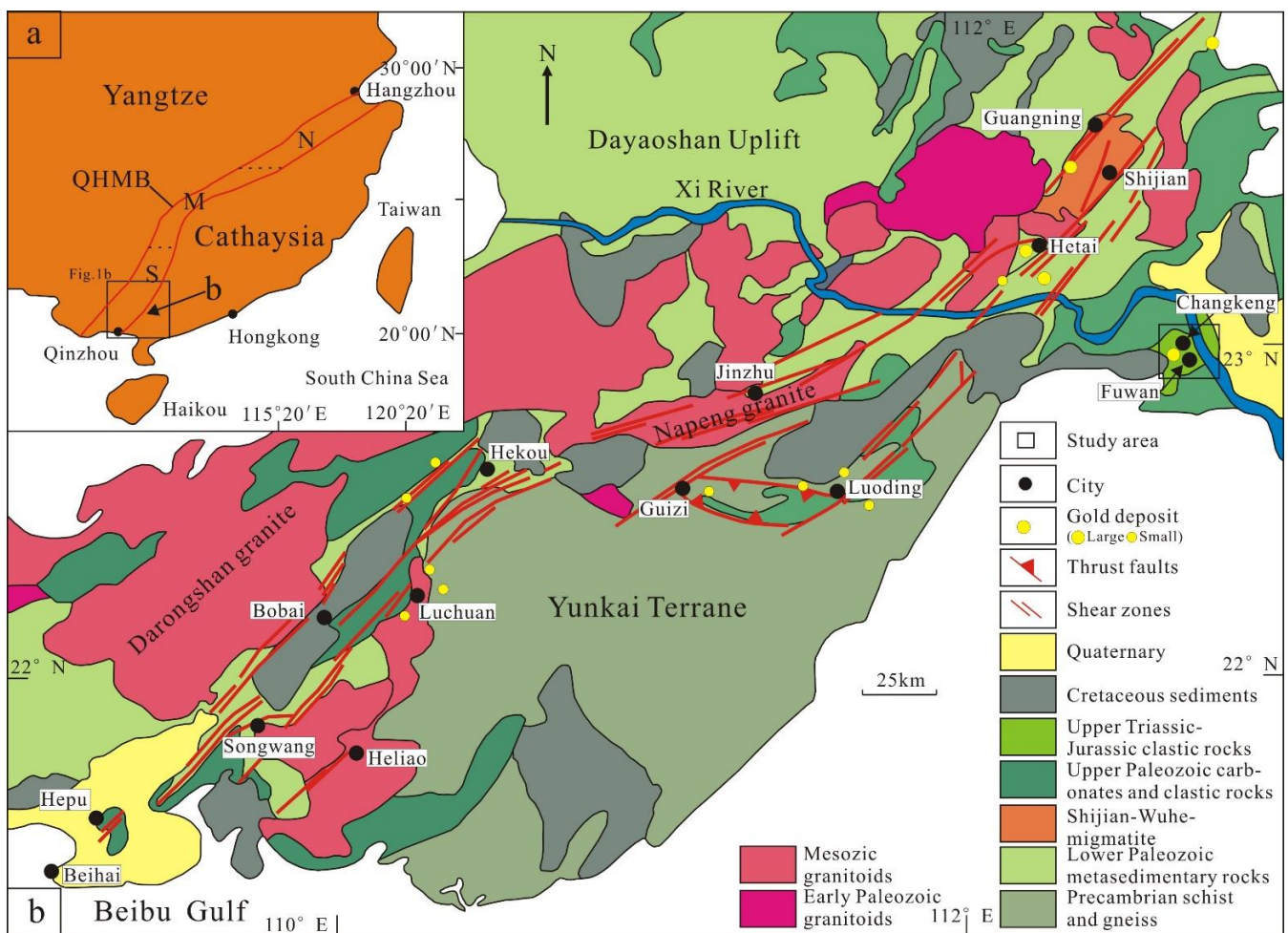


**Figure 1.** (a) Location of the QHMB in the South China Block (modified from [4,38]). (b) Geological sketch map of the southern segment of the QHMB (modified from [36]). The locations of the gold deposits are from reference [50].

The Sanshui Basin, which hosts the Changkeng–Fuwan Au–Ag deposit, is situated in the northwest of West Guangdong–East Guangxi (Figure 2). It is typical of a Mesozoic–Cenozoic extensional basin with an area of approximately 3300 km<sup>2</sup>. The outcropping rocks in the basin consist of metamorphic rocks (Neoproterozoic to Ordovician metasedimentary sequences), Paleozoic and Mesozoic sedimentary rocks, Mesozoic granite, and late Cretaceous to Cenozoic cover rocks [51] (Figure 2). The basement rocks are unconformably overlain by middle Devonian to early Carboniferous marine sedimentary rocks and include sandstone and siltstone [15]. The Mesozoic to Cenozoic continental sedimentary clastic rocks unconformably overlay the lower Carboniferous limestone and are overlain by Eocene volcanic rocks [15]. The Eocene volcanic and sedimentary rocks consist mainly of basalt, rhyolite, tuff, trachytic tuff, and pyroclastic agglomerate [15]. There are mainly five groups of faults with directions of NE-, WE-, and NW-trending, which contain the Wuchuan–Sihui, Enping–Conghua, Xijiang, Panyu, and Shougouling faults (Figure 2). The activities of the large and deep faults in the area provided favorable channels and spaces for the transportation and precipitation of ore-forming fluids. Many Au–Ag–Pb–Zn polymetallic mineralizations, such as the Luzhou, Dieping, Chashan, Hengjiang, and Xiqiaoshan deposits, are closely correlated with the volcanic–hydrothermal and post-magmatic hydrothermal processes in the Sanshui Basin (Figure 2).

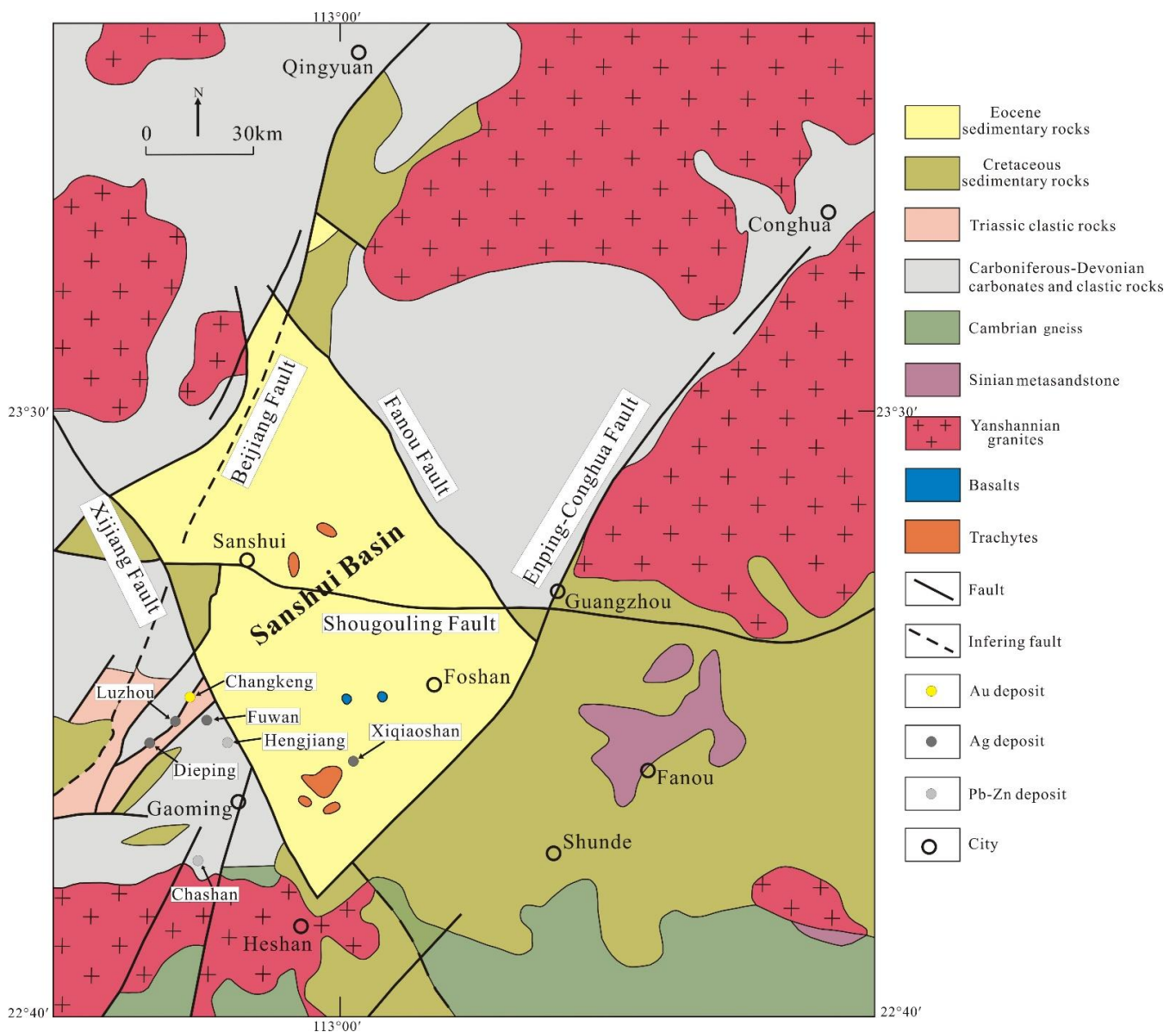


**Figure 2.** Geological sketch map of the Sanshui basin with the deposits (modified from [52]).

### 3. Deposit Geology

The Changkeng–Fuwan Au–Ag deposit is located approximately 15 km northwest of Gaoming County, Guangdong Province (Figure 2). The Au and Ag orebodies are hosted in the same altered fracture zone, forming independent gold and silver orebodies, respectively, with the characteristics of “upper gold and lower silver” in space. The exposed strata are the Carboniferous Zimenqiao, Ceshui and Shidengzi Formations, Triassic Xiaoping Formation, Cretaceous Baizushan Formation, and overlying Tertiary and Quaternary [15] (Figure 3a). The Zimenqiao, Ceshui, and Shidengzi Formations are sparsely distributed in the northwestern margin of the deposit and are composed predominantly of bioclastic and silty limestone [15]. The Zimenqiao formation shows the fault contact with the Xiaoping Formation. The Xiaoping Formation covers the entire central part of the deposit and unconformably overlies the Baizushan Formation. The Baizushan Formation, exposed in the northeast of the deposit, is composed predominantly of clastic rocks containing conglomerate, sandstone (fine sandstone and siltstone), and mudstone.

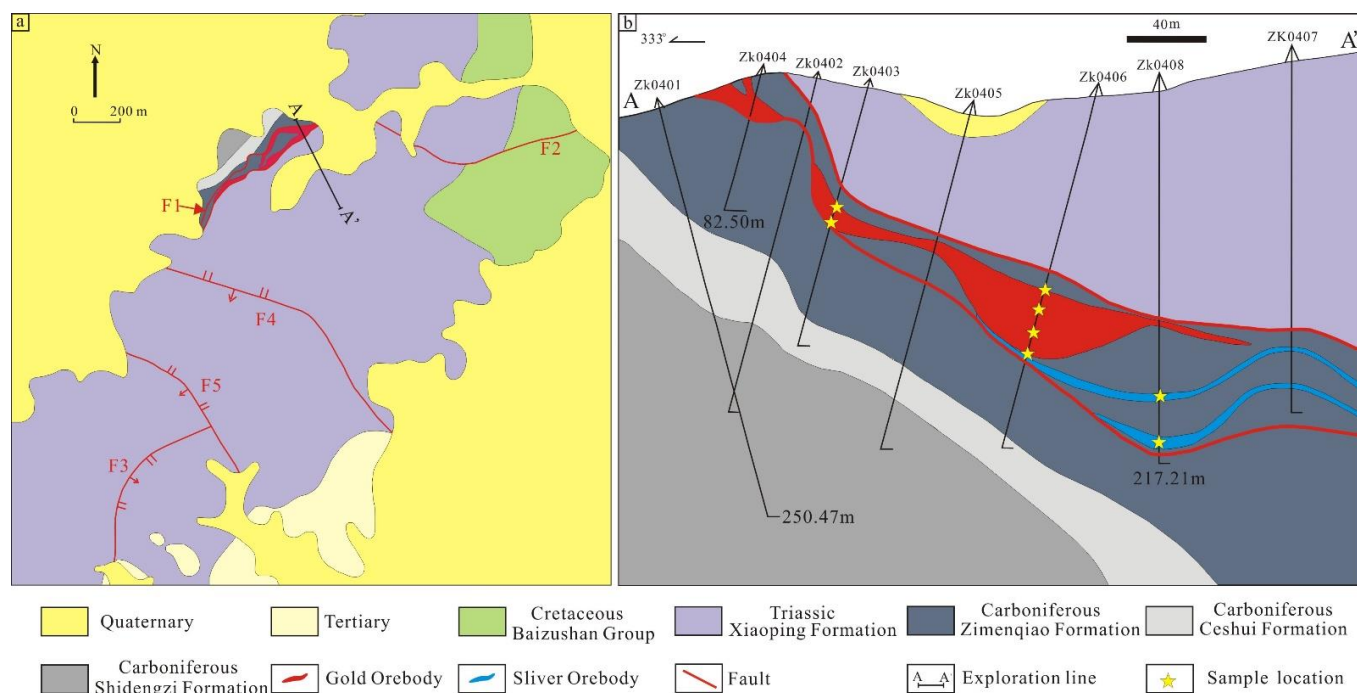


**Figure 3.** Geological sketch map (a) and geological cross section (b) of the Changkeng–Fuwan Au-Ag deposit (modified from [15]).

Structurally, the NW-trending and NE-trending faults are widely distributed in the Changkeng–Fuwan Au-Ag deposit (Figure 3a). The NE-trending fault (F1) is the major ore-controlling fault, with the trending from 30 to 60°, dipping at angles of 10–35° SE. The NW-trending (F4, F5) and NE-trending (F3) faults cut across the orebodies, which formed after the mineralization. Although there are no exposures of igneous rocks at the surface in the mining district, related geophysical data showed that there may be concealed pluton underlying the deposit [16].

### 3.1. Characteristics of the Orebodies and Ore Mineral Assemblages

The Au and Ag orebodies of the Changkeng–Fuwan deposit occur as stratiform, stratoid, and lenticular shapes and are hosted in the Zimenqiao Formation (Figure 3b). The Au orebody is hosted in the siliceous rocks, while the Ag orebody is hosted in the limestone. The Au and Ag orebodies were mainly controlled by the F1 fault. The Au orebody is located in the north of the mining area and at the upper stratigraphic section, whereas the Ag orebody is located in the south of the mining area and at the lower stratigraphic section (Figure 3b). Two Au orebodies in total were developed during the Au mineralization; almost all metallogenetic features were documented by the largest No.1 orebody, which is more than 750 m length and 1–40 m (average of 10 m) thickness and has an average grade of 7.94 g/t Au. It strikes NEE and dips to the SSE at 30–50°. There were five Ag orebodies developed during the Ag mineralization, and the largest (No. 1) orebody appeared as stratiform, characterized by approximately 2318 m in length and 0.3–32.2 m (average 4.7 m) in thickness, with an average Ag grade of 225.93 g/t. The No. 1 Ag orebody strikes 30–60° SW and dips 10–30° SE.

The content of the metal sulfides in the Au orebody is low, and pyrite is the most abundant mineral. Minor sulfides include sphalerite and chalcopyrite (Figures 4 and 5c,d), and none of these minerals contain appreciable concentrations of Au. The gangue minerals mainly include quartz, sericite, and calcite, with minor realgar and fluorite (Figures 4 and 5a,f,g). The Au occurs as submicroscopic (<0.1 μm) grains in fissures of pyrite, quartz, and clay minerals [20]. The ore minerals of the Ag orebody predominantly include pyrite, galena, sphalerite, and silver-bearing minerals, with minor chalcopyrite (Figure 5i–k); while the gangue

minerals are mostly quartz, sericite, and calcite (Figure 5h,l), with accessory fluorite. The Ag-bearing minerals mainly include freibergite, pyrargyrite, and andorite, which usually are intergrown with galena and sphalerite (Figure 5j).

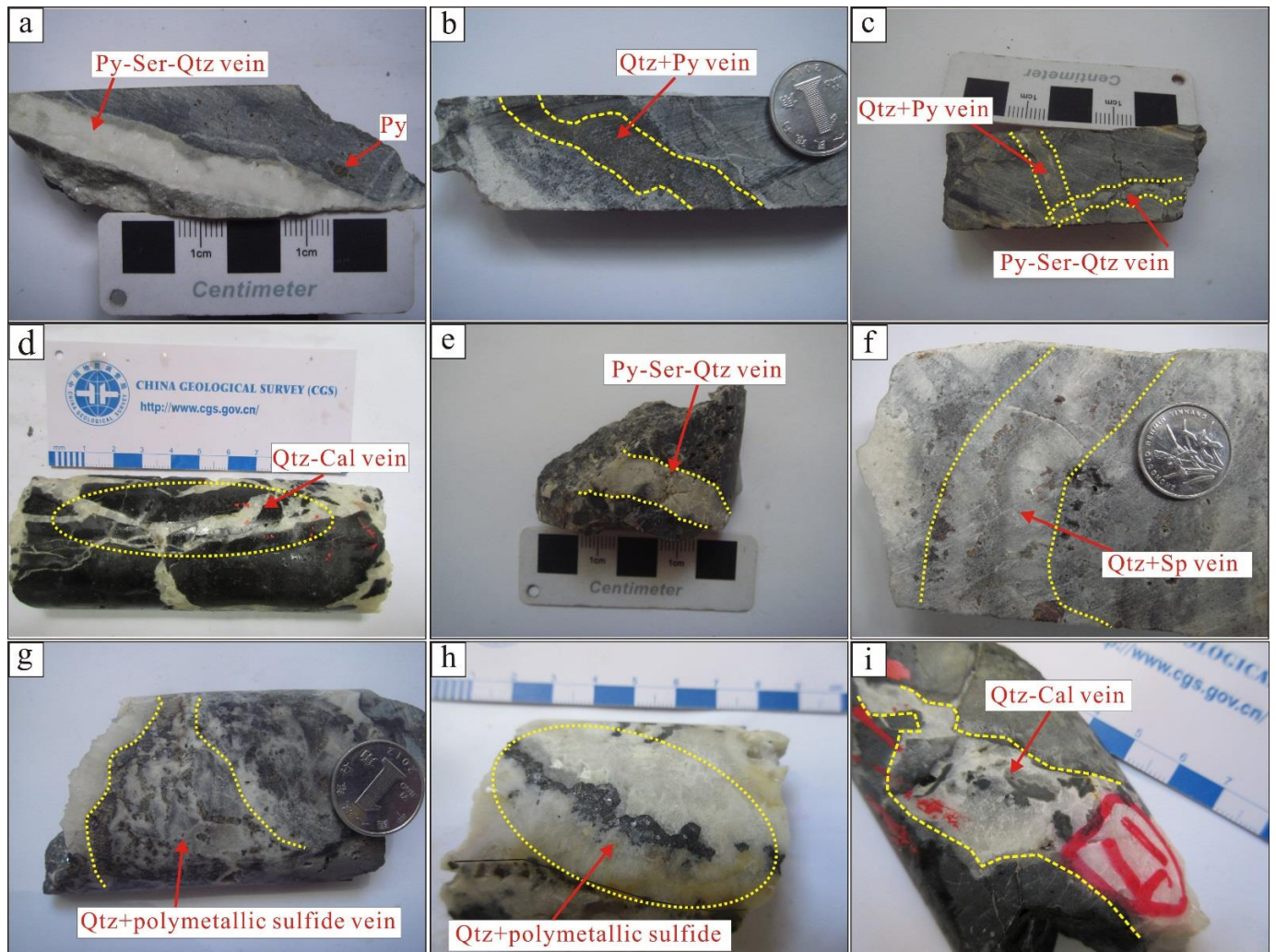


**Figure 4.** Photographs of different stages in the Changkeng–Fuwan Au (a–d)–Ag (e–i) deposit. (a) Pyrite–sericite–quartz in the early stage; (b) pyrite–quartz vein in the middle stage; (c) early stage pyrite–sericite–quartz vein cut by middle-stage quartz–pyrite vein; (d) quartz–carbonate vein in the late stage; (e) pyrite–sericite–quartz in the early stage; (f) quartz and sphalerite in the middle stage; (g,h) quartz–polymetallic sulfide vein in the middle stage; and (i) quartz–carbonate vein in the late stage. Py, pyrite; Sp, sphalerite; Qtz, quartz; Ser, sericite; and Cal, calcite.

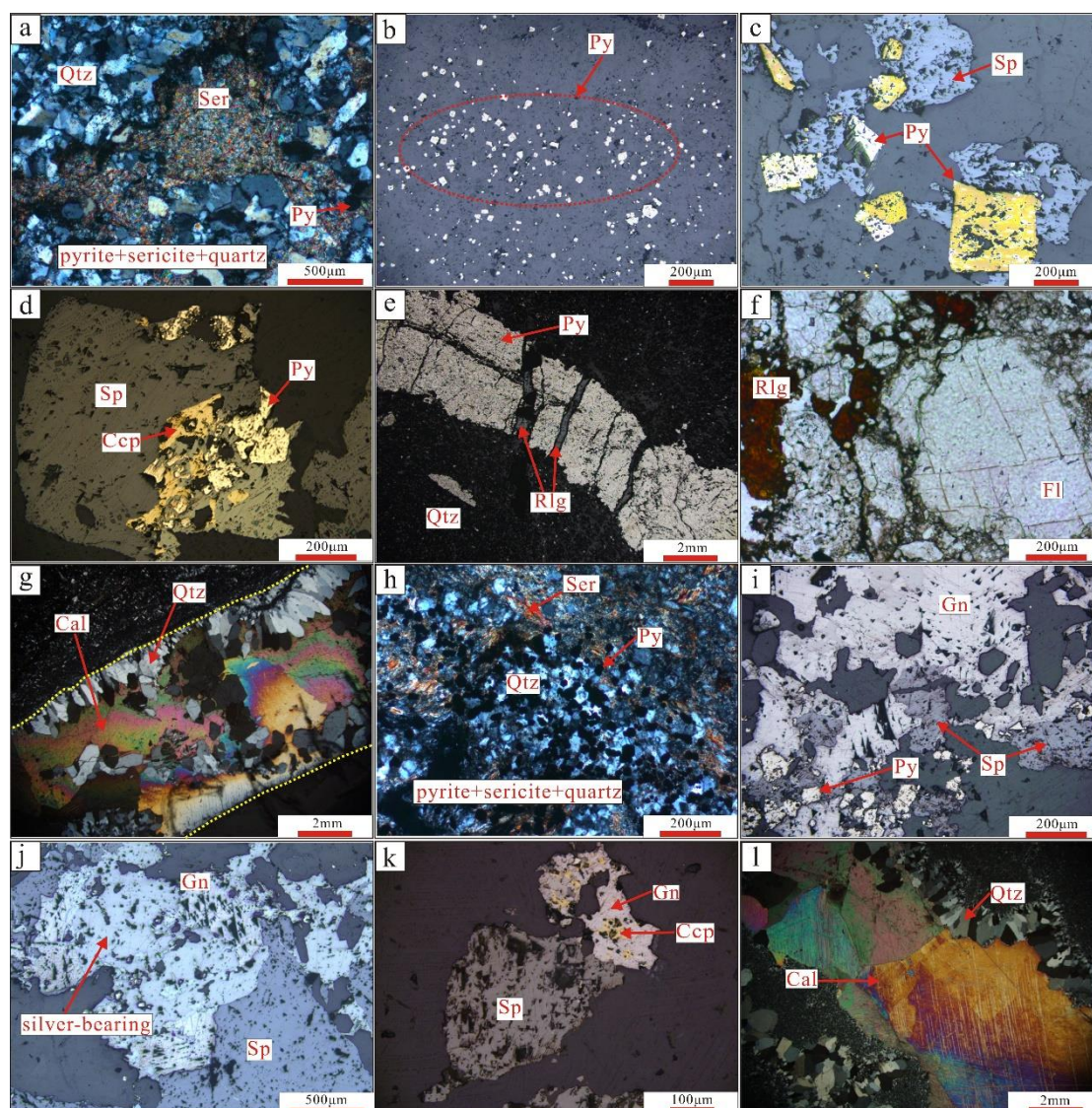


**Figure 5.** Photomicrographs showing the mineral assemblages and the alteration of different stages in the Changkeng–Fuwan Au (a–g)–Ag (h–l) deposit. (a,f,g,h,l) Transmitted light, (b–e,i–k) reflected light). (a) Early stage pyrite + sericite + silica alteration; (b) euhedral to subhedral pyrite; (c) middle stage sphalerite; (d) galena, sphalerite, and chalcopyrite in the middle stage; (e) middle stage pyrite cut by late stage realgar; (f) realgar and fluorite in the late stage; (g) quartz and calcite vein in the late stage; (h) early stage pyrite + sericite + silica alteration; (i) middle stage galena and sphalerite replacing pyrite; (j) silver-bearing mineral intergrowth with galena and sphalerite in the middle stage; (k) galena, sphalerite, and chalcopyrite in the middle stage; and (l) quartz and calcite vein in the late stage. Py, pyrite; Gn, galena; Ccp, chalcopyrite; Sp, sphalerite; Qtz, quartz; Ser, sericite; Rlg, realgar; and Cal, calcite.

### 3.2. Hydrothermal Alteration and Mineralization Stages

The hydrothermal alteration associated with the Au and Ag mineralization is similar. The main alteration types consist of silicification, sericitization, sulfidation, and carbonatization. Among these, silicification and sulfidation are the most common types. Silicification manifested as quartz–pyrite, quartz–polymetallic sulfide, and quartz–carbonate veins (Figure 4a,b,d,h,i). Sericitization mainly manifested as scaly aggregates (Figure 5a,h). Pyrite is closely related to the silicic and sericitic alteration (Figure 5a,h). Carbonation mainly occurred as quartz–carbonate veins (Figure 4d,i and Figure 5g,l). The mineralogy and associated wall rock alteration of each stage are summarized briefly below (Figure 6).

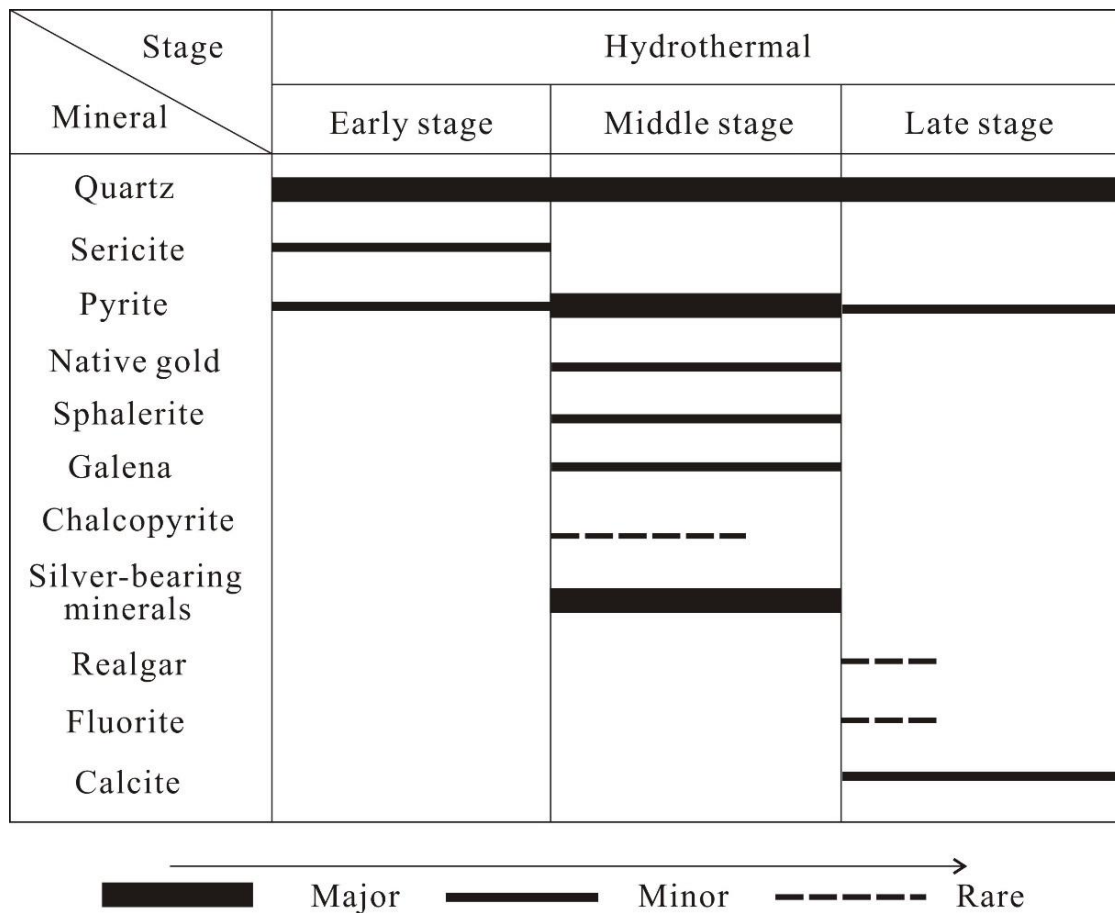


**Figure 6.** Paragenetic sequence for major minerals of the Changkeng–Fuwan Au-Ag gold deposit.

Three metallogenic stages have been identified in the Changkeng–Fuwan Au-Ag deposit (Figure 4). The early stage of the Au mineralization is represented by pyrite–sericite–quartz alteration rocks (Figures 4a and 5a). The ore minerals mainly consisted of pyrite, which was sparsely disseminated in grained and euhedral to subhedral crystals (Figure 5b,c). The gangue minerals mainly consisted of quartz and sericite (Figure 5a). The quartz during this stage was mainly chalcedony, and its grains were subhedral crystals or anhedral crystals (Figure 5a). Sericite showed scaly aggregates and was intergrown with pyrite and quartz (Figure 5a). The middle stage consists of quartz–pyrite veins (Figure 4b,c), which is the most important stage of gold production. It contained quartz and pyrite. Most of the quartz was smoky grey, fine-grained, with euhedral and subhedral crystals, and the pyrite was fine-grained. The late stage is characterized by quartz + calcite (Figures 4d and 5g).

The early stage of the Ag mineralization is also characterized by pyrite–sericite–quartz altered rocks (Figures 4e and 5h). The ore mainly comprised quartz, sericite, and minor pyrite (Figure 5h). The quartz was mainly chalcedony, and its grains were subhedral crystals or anhedral crystals (Figure 5h). The pyrite grains were fine-grained and euhedral–subhedral crystal and were disseminated in sericite and quartz (Figure 5h). The middle stage includes quartz–polymetallic sulfide veins (Figure 4f–h), which is the most significant stage of Ag production. The ore minerals consisted of pyrite, sphalerite, galena, and silver-bearing minerals (Figure 5i–k). The pyrite was fine-grained, and other sulfides formed the bulk of the ore (Figure 5i). Quartz made up the main gangue mineral. The polymetallic sulfides and Ag-bearing minerals showed a close relationship (Figure 5j). The late stage is represented by a large amount of calcite and quartz (Figures 4i and 5l).

## 4. Samples and Methods

### 4.1. Fluid Inclusion Microthermometry

In total, 46 doubly polished thin sections (21 samples from the Au orebody and 25 samples from the Ag orebody) representing different stages were selected for the FIs studies. Based on the detailed petrography, 8 samples (early stage, 3; middle stage, 3; and late stage, 2) from the Au orebody and 11 samples (early stage, 4; middle stage, 5; and late stage, 2) from the Ag orebody were selected for microthermometric measurements and Laser Raman spectroscopic analyses. The microthermometric measurements were conducted at the China University of Geosciences Beijing, using a LINKAM THMGS-600 heating–freezing stage, with a measured temperature range of  $-190$  °C to  $+600$  °C. The accuracy of the measurements was ensured by calibration at  $-56.6$  °C and  $0$  °C, using synthetic fluid inclusion standards and pure water. The heating rates were  $0.1$  °C/min when phase transitions were approached. The errors were about  $\pm 0.2$  °C for the final ice melting temperatures and  $\pm 5$  °C for the homogenization temperatures. Laser Raman spectroscopic analyses were conducted on a LABHR-VIS LabRAM HR800 microspectrometer at the Beijing Geological Research Institute of Nuclear Industry, China. The wavelength of the argon ion laser was 532 nm. The scanning range for the spectra lay between 100 and  $4000$   $\text{cm}^{-1}$ , with an accumulation time of 10 s for each scan and a spectral resolution of  $1\text{--}2$   $\text{cm}^{-1}$ . The detailed procedures followed those reported in previous studies [53–56].

### 4.2. Isotope Analyses

In total, 33 representative samples across the three identified ore mineralization stages were selected for isotope analysis (C, H, O, S, Pb, He, and Ar), which was performed at the Beijing Geological Research Institute of Nuclear Industry, China. Fifteen quartz samples from three different stages of the Au and Ag orebodies were selected for H–O isotopic analyses. Before measurement, the samples were heated in an induction furnace under a vacuum and high temperature ( $\sim 130$  °C) condition, in order to eliminate the absorbed water in the minerals. Oxygen was liberated by reaction with  $\text{BrF}_5$  and converted to  $\text{CO}_2$  on a platinum-coated carbon rod [57]. Hydrogen was released by reaction with  $\text{CuO}$  to generate  $\text{H}_2\text{O}$ , which then was reduced to  $\text{H}_2$  through the Zn catalyst method [58]. The isotopic compositions of both gases were analyzed on a Finnigan MAT253 mass spectrometer.

Sulfur isotopic analyses were conducted on five pyrite, two realgar, and two sphalerite samples, including two realgar samples and one pyrite sample from the Au orebody and four pyrite and two sphalerite samples from the Ag orebody. The samples were analyzed for sulfur isotope using a Finnigan MAT 251 mass spectrometer. The precision for  $\text{d}^{34}\text{S}$  was better than  $\pm 0.2\text{‰}$  [59].

Six samples including pyrite and sphalerite were chosen for Pb isotopic determinations. The samples were dissolved in a mixed solution of hydrofluoric acid and perchloric acid, followed by basic anion exchange resin to purify the Pb. Pb isotopic compositions were determined by using an ISOPROBE-T Thermal Ionization Mass Spectrometer instrument, and the precisions were better than 0.005%.

Four pyrite, three sphalerite, and one galena separate were selected for He–Ar isotopic analyses. These sulfide grains were cleaned ultrasonically in alcohol, dried, and loaded on-line in vacuo crushers. The sample chips were baked at  $100\text{--}150$  °C for 24 h in order to remove the adsorbed atmospheric contaminants before analyses; then, gases were extracted from the fluid inclusion by crushing in a vacuum. He and Ar isotopic compositions of the inclusion-trapped fluids were measured by using a HelixSFT mass spectrometer.

C–O isotopic analyses were performed on nine calcite samples, including three calcite samples from the Au orebody and six calcite samples from the Ag orebody. C–O isotopic compositions of the nine calcite samples were obtained by using an automatic Multiprep sample preparation device attached to a GV IsoPrime II mass spectrometer. Calcite reacts with 100% phosphoric acid ( $\text{H}_3\text{PO}_4$ ) to produce  $\text{CO}_2$ . The analytical precision (2 $\sigma$ ) was  $\pm 0.1\text{‰}$  for  $\delta^{13}\text{C}$  and  $\pm 1\text{‰}$  for  $\delta^{18}\text{O}$  [60].

## 5. Results

### 5.1. Fluid Inclusion Study

Although there were many fluid inclusions (FIs) in the samples, they were too small to determine the phase change. Therefore, only the large isolated primary FIs were selected for measurement. The classification of the primary and secondary FIs was according to Lu et al. [54] and Roedder [61]. Based on the phase compositions at room temperature and the phase transitions (Figure 7), two types of FIs were recognized: two-phase liquid-rich inclusions (type I) and monophasic liquid inclusions (type II).

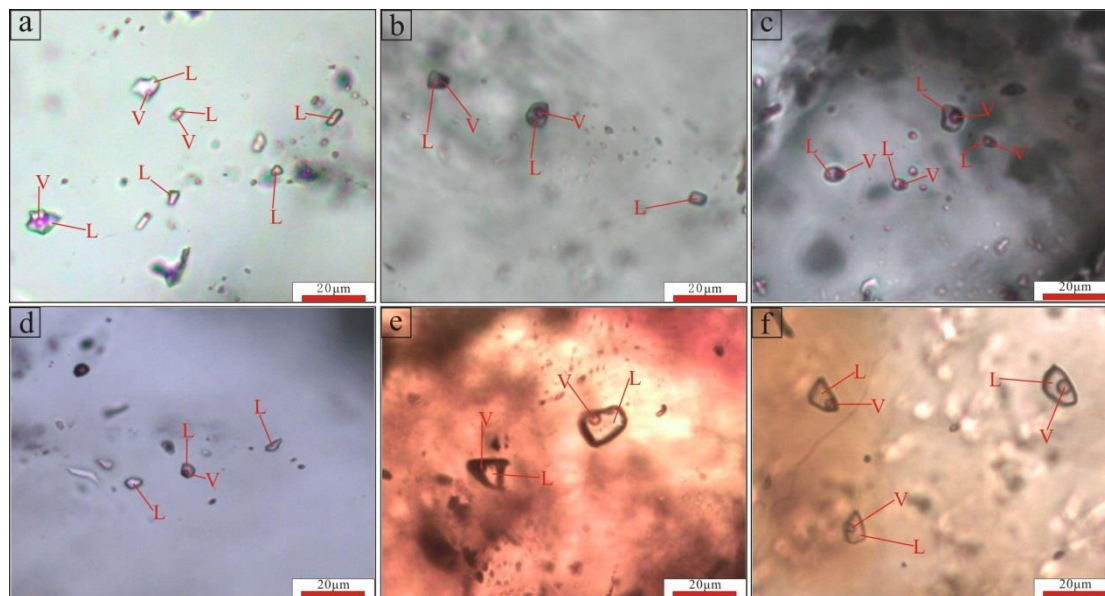


**Figure 7.** Photomicrographs of various types of fluid inclusions observed in the Changkeng–Fuwan Au (a–c) and Ag (d–f) deposit.

The type I FIs commonly contain a vapor bubble and liquid phase at room temperature. The vapor phase occupies the fluid inclusion volume from 5 to 30%, and the phase status at homogenization is liquid phase. These inclusions are round or irregular in shape, and their size varies from 3 to 12  $\mu\text{m}$ . Type I FIs were more abundant in all the samples and widely distributed. Type II FIs consist of a brine liquid, and their diameters are 2–5  $\mu\text{m}$ . Type II FIs were relatively rare and only found in the late stage quartz veins, coexisting with type I FIs (Figure 7).

### 5.2. Microthermometry

The main microthermometric results of the FIs are listed in Table 1. Figures 7 and 8 show the statistical distribution as histograms.

#### 5.2.1. Microthermometry of the Au Orebody

**Early Stage:** the quartz from the early stage only contained type I inclusions. The Th values of the type I inclusions varied from 223  $^{\circ}\text{C}$  to 282  $^{\circ}\text{C}$ . The ice-melting temperatures varied from  $-6.6$   $^{\circ}\text{C}$  to  $-1.2$   $^{\circ}\text{C}$ , which yielded salinities from 2.1 to 9.9 wt.% NaCl equiv. (Table 1, Figure 8a,b).

**Middle stage:** this stage also only contained type I inclusions in the quartz, which yielded ice-melting temperatures ranging from  $-6.5$   $^{\circ}\text{C}$  to  $-1.1$   $^{\circ}\text{C}$ , with corresponding salinities from 1.9 to 9.9 wt.% NaCl equiv. The Th values varied from 187  $^{\circ}\text{C}$  to 231  $^{\circ}\text{C}$  and had a peak between 200  $^{\circ}\text{C}$  and 210  $^{\circ}\text{C}$  (Table 1, Figure 8c,d).

**Late stage:** this stage was dominated by type I inclusions in the quartz and calcite, with some type II inclusions. The type I inclusions in the calcite were analyzed. The ice-melting temperatures ranged from  $-1.8$   $^{\circ}\text{C}$  to  $-0.2$   $^{\circ}\text{C}$ , with the corresponding salinities varying

from 0.4 to 3.1 wt.% NaCl equiv. The Th values ranged from 158 to 211 °C and had a peak in the range of 170–190 °C (Figure 8e,f).

**Table 1.** Microthermometric data of FIs in the Changkeng–Fuwan Au–Ag deposit.

Orebody	Host Mineral	Stage	Type	N	Size/ $\mu\text{m}$	Th/ $^{\circ}\text{C}$	T <sub>m-ice</sub> / $^{\circ}\text{C}$	wt.%NaCl.eqv	
						Range	Range	Range	Mean
Gold orebody	Quartz	Early	L + V	49	4–10	223–282	245	−6.6–−1.2	6.1
	Quartz	Middle	L + V	46	3–8	187–231	204	−6.5–−1.1	5.3
	Calcite	Late	L + V	49	3–6	158–211	184	−1.8–−0.2	1.4
Silver orebody	Quartz	Early	L + V	48	4–12	210–289	236	−8.0–−2.0	7.4
	Quartz	Middle	L + V	49	5–14	180–232	206	−6.5–−1.1	7.3
	Sphalerite	Middle	L + V	17	6–14	187–230	209	−8.8–−2.2	7.0
	Calcite	Late	L + V	36	4–10	146–203	176	−1.0–−0.1	0.7

Notes: N, number of inclusions analyzed; Th, homogenization temperature; T<sub>m-ice</sub>, ice-melting temperature; wt.%NaCl.eqv, salinity; L, liquid; V, vapor.

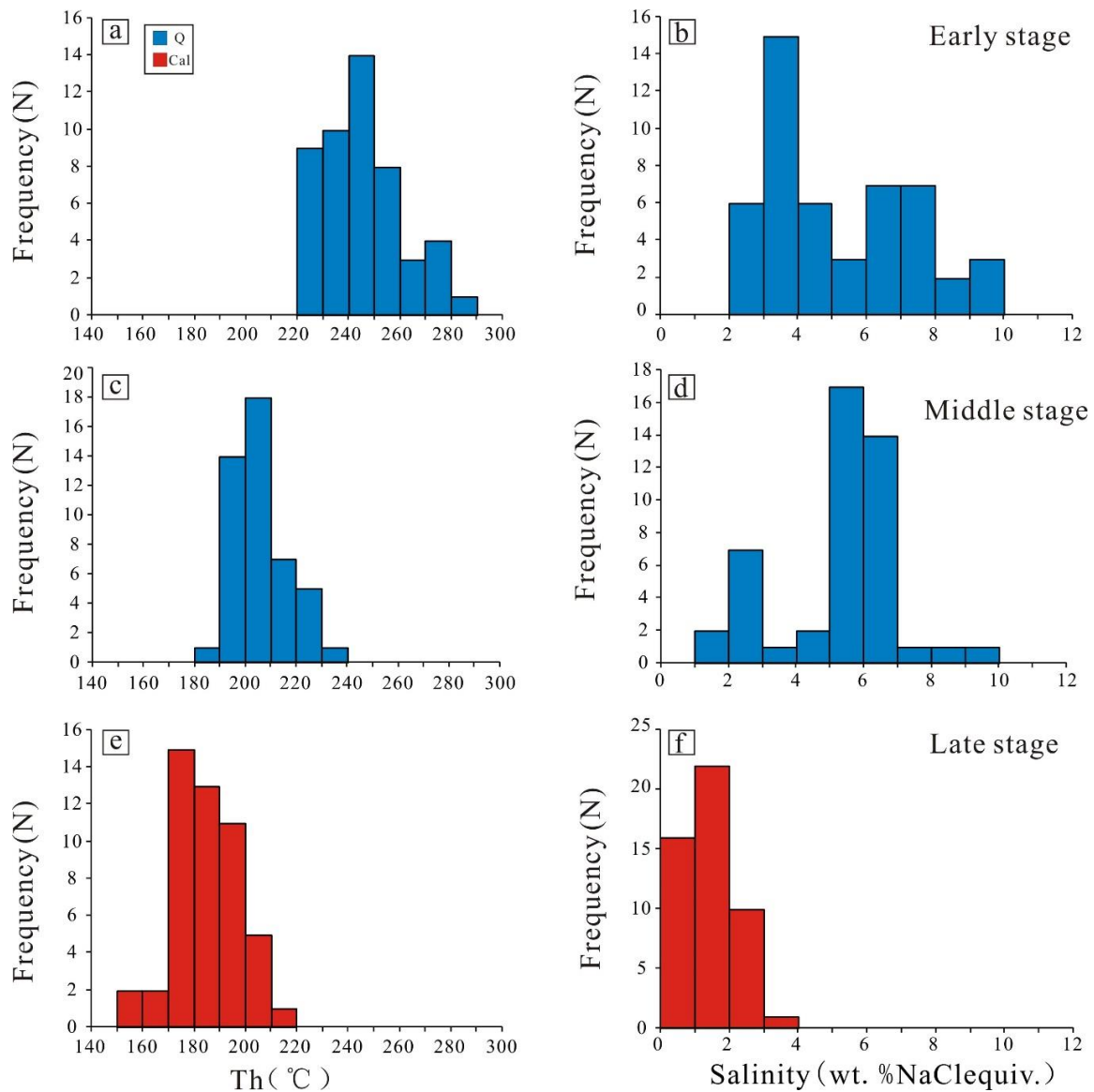


**Figure 8.** Frequency histograms of the total homogenization temperatures (Th) and salinities of the fluid inclusions from different stages of the Changkeng–Fuwan Au deposit. Early stage (a,b); middle stage (c,d) and late stage (e,f). Qtz, quartz; Cal, calcite.

### 5.2.2. Microthermometry of the Ag Deposit

Early Stage: the quartz from the early stage only contained type I inclusions. The Th values varied from 210 °C to 289 °C. The ice-melting temperatures ranged from −8.0 °C to −2.0 °C, which yielded salinities from 2.4 to 11.7 wt.% NaCl equiv. (Table 1, Figure 9a,b).

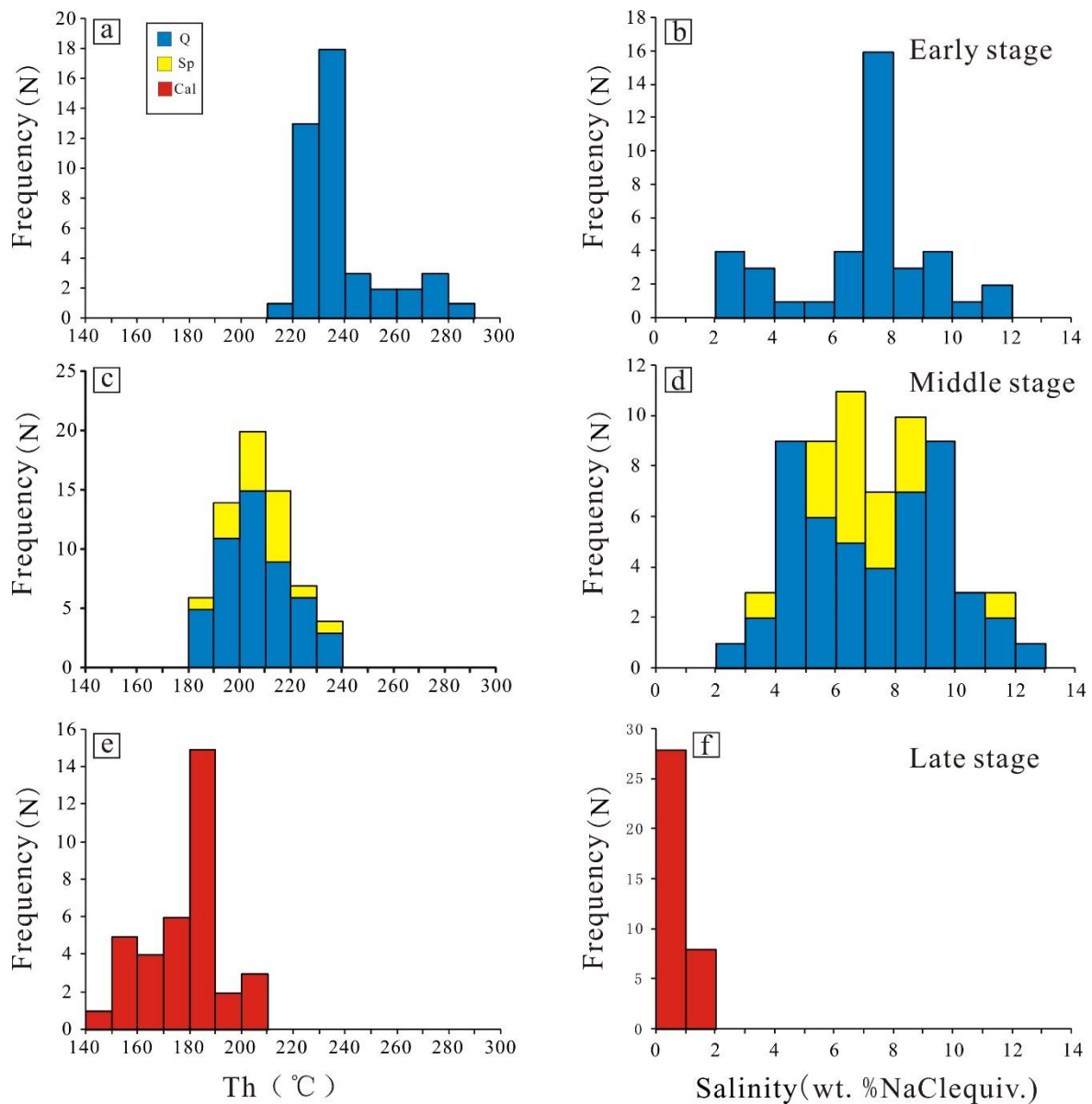


**Figure 9.** The frequency histograms of the total homogenization temperatures (Th) and salinities of the fluid inclusions from different stages of the Changkeng–Fuwan Ag deposit. Early stage (a,b); middle stage (c,d) and late stage (e,f). Qtz, quartz; Cal, calcite; Sp, sphalerite.

Middle stage: this stage also only contained type I inclusions in the quartz and sphalerite. The ice-melting temperatures from the quartz ranged from −6.5 to −1.1 °C, with corresponding salinities from 2.6 to 12.4 wt.% NaCl equiv. The Th values varied from 180 °C to 232 °C and had a peak between 200 °C and 210 °C. The ice-melting temperatures from the sphalerite varied from −8.8 °C to −2.2 °C, with corresponding salinities from 3.7 to 12.6 wt.% NaCl equiv. The Th values ranged from 187 °C to 230 °C (Table 1, Figure 9c,d).

Late stage: this stage was dominated by type I inclusions in the quartz and calcite, with some type II inclusions. The type I inclusions in calcite were analyzed from this stage. The

ice-melting temperatures ranged from  $-1.0$  to  $-0.1$  °C, with corresponding salinities from 0.2 to 1.7 wt.% NaCl equiv. The Th values varied from 146 to 203 °C (Table 1, Figure 9e,f).

### 5.3. Laser Raman Spectroscopy

We used laser Raman spectroscopy to detect the composition of the FIs in quartz. The peak value of the water in the Raman analysis was 2800–3800 cm [62]. The results revealed that the vapor and liquid phases of the FIs comprised H<sub>2</sub>O (Figure 10), and no other volatiles were determined.

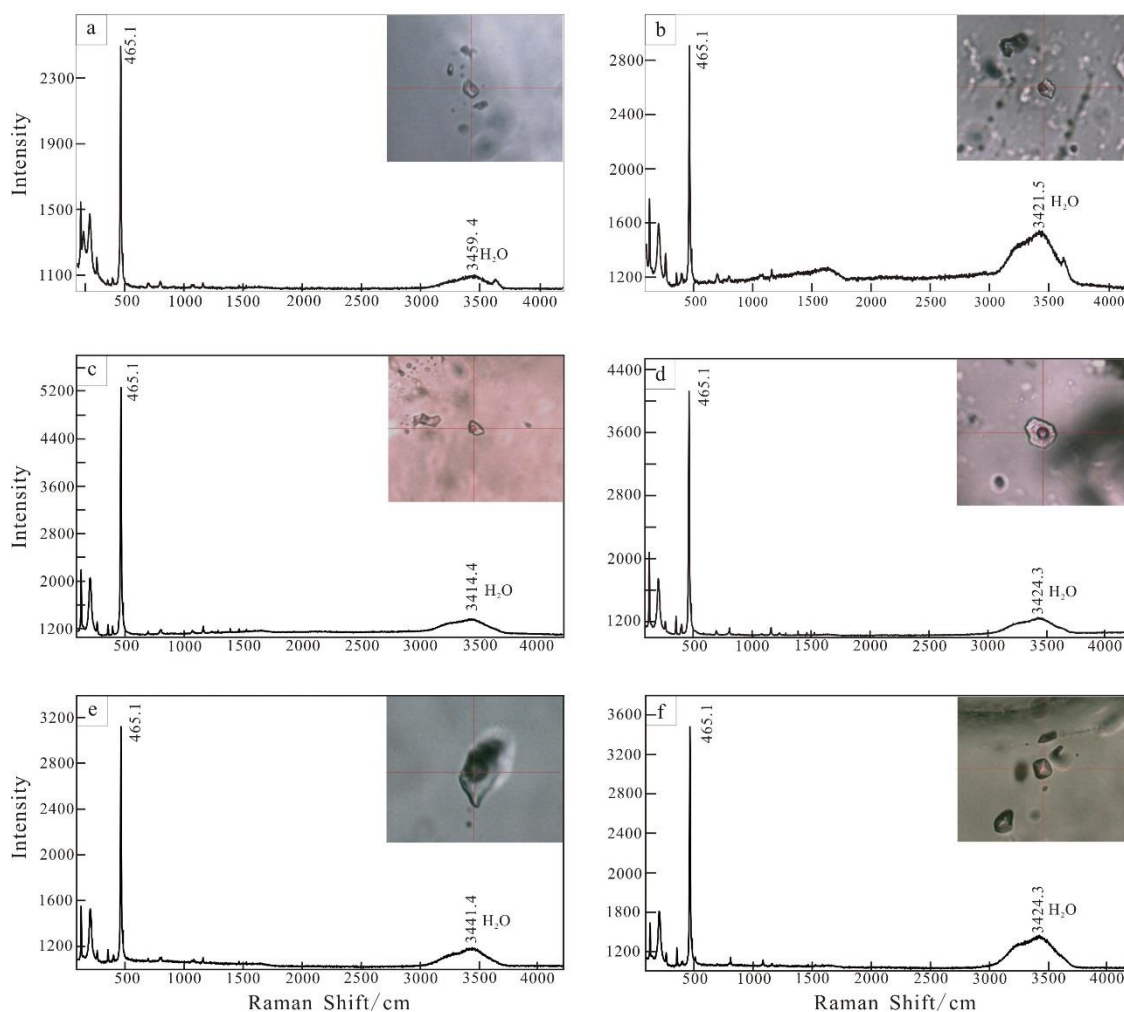


**Figure 10.** Laser Raman analyses of representative FIs from the Changkeng–Fuwan Au (a,c,e)-Ag (b,d,f) deposit.

### 5.4. H and O Isotopes

The H and O isotopic data at different stages with historical data are presented in Table 2. The  $\delta D$  values of the FIs in the Au orebody ranged from  $-84.1$  to  $-46.0$ ‰ (average  $-64.9$ ‰). The  $\delta^{18}O_{V-SMOW}$  values varied from 10.5 to 13.8‰. The corresponding values in the Ag orebody were  $-89.0$  to  $-55.3$ ‰ (average  $-71.9$ ‰) and 8.8 to 13.0‰, respectively. The O isotope composition of the hydrothermal water was characterized by an  $\delta^{18}O_{H_2O}$  value, which was calculated by the equation  $(1000 \ln \alpha_{\text{quartz-water}} = 3.38 \times 10^6 T^{-2} - 3.40)$  of Clayton et al. [63] and Jiao et al. [8]. The  $\delta^{18}O_{H_2O}$  values for the fluids in the Au orebody varied from  $-2.16$  to 2.46‰ (mean 0.06‰). The corresponding values in the Ag orebody were  $-1.38$ –3.66‰ (mean 1.20‰).

**Table 2.** H and O isotope data of different stages from the Changkeng–Fuwan Au–Ag deposit.

Orebody	Sample	Mineral	Stage	Th (°C)	$\delta^{18}\text{O}_{\text{V-SMOW}}$ ‰	$\delta^{18}\text{O}_{\text{H}_2\text{O}}$ ‰	$\delta\text{D}_{\text{V-SMOW}}$ ‰	Reference
Gold orebody	CKP31-1	Quartz	I	238	12	2.46	−72.6	This study
	CKP5-3	Quartz	I	240	11.6	2.16	−56.5	
	CKP11-1	Quartz	II	201	12.3	0.67	−84.1	
	CKP2-3	Quartz	II	208	10.5	−0.7	−65.7	
	G0305-7	Quartz	III	178	13.8	0.64	−57	[20]
	G0405-9	Quartz	III	178	11	−2.16	−78	
	G0406-19	Quartz	III	178	11.8	−1.36	−60	
	G3210	Quartz	III	187	11.9	−1.26	−46	
Silver orebody	CKP16-2	Quartz	I	263	8.8	0.44	−87.7	This study
	CKP32-17	Quartz	I	242	10.7	1.36	−55.3	
	CKP22-1	Quartz	I	242	10.7	1.36	−65.3	
	CKP34-20	Quartz	I	242	11.4	2.06	−60.1	
	CKP5-5	Quartz	I	242	12.3	2.96	−77.7	
	CKP31-3	Quartz	I	242	13	3.66	−79.5	
	CKP11-2	Quartz	II	224	8.9	−1.38	−77.1	
	CKP17-2	Quartz	II	209	12.2	1.06	−66.6	
	CKP14-2	Quartz	II	208	12.4	1.2	−67	
	CKP36-4	Quartz	II	208	12.1	0.9	−89.6	
	CKP33-23	Quartz	III	203	11.6	0.09	−64.8	

Th is the mean homogenization temperature.

### 5.5. S and Pb Isotopes

The sulfur isotopic data from the Au and Ag orebodies are shown in Tables 3 and 4. The  $\delta^{34}\text{S}$  values of sulfides from the Au and Ag orebodies ranged from −5.80 to 8.73‰ (mean −0.84‰) and −8.70 to 7.39‰ (mean 2.58‰), respectively. In the Au orebody, the pyrite showed  $\delta^{34}\text{S}$  values of −5.80 to 8.73‰ (mean −1.25‰), the stibnite had  $\delta^{34}\text{S}$  values ranging from −3.90 to 2.30‰ (mean 0.07‰), and the realgar displayed a range from 1.30 to 5.30‰ (mean 3.76‰). In the Ag orebody, the pyrite showed  $\delta^{34}\text{S}$  values of −8.70 to 6.41‰ (mean 0.79‰), the galena had  $\delta^{34}\text{S}$  values ranging from 0.07 to 5.61‰ (mean 2.54‰), and the sphalerite displayed a range from 1.70 to 7.39‰ (mean 3.92‰). Overall, the  $\delta^{34}\text{S}$  values of the sulfides from the Au and Ag orebodies were similar, with a pronounced normal distribution.

**Table 3.** S isotope data of the sulfides from the gold orebody.

Sample	Mineral	$\delta^{34}\text{S}_{\text{V-CDT}}$ (‰)	Reference
ck-19	Pyrite	−0.3	[64]
ck-38	Pyrite	−5.2	
ck-147	Pyrite	−5.3	
ck-55	Stibnite	−3.9	
ck-33	Stibnite	2.3	
ck-39	Stibnite	0.8	
ck-145	Stibnite	2.2	
G0802-8	Pyrite	−2.2	[65]
G0802-9	Pyrite	−1.9	
G0001-5	Pyrite	−5.8	
G0405-12	Pyrite	−0.8	
K01-1	Pyrite	−3.1	

Table 3. Cont.

Sample	Mineral	$\delta^{34}\text{S}_{\text{V-CDT}}(\text{‰})$	Reference
CKZK-1	Pyrite	−2.2	
CK-5	Stibnite	2.01	
N334	Stibnite	−1.23	
CK-25	Stibnite	−1.95	[21]
CKIA-4	Stibnite	−0.56	
CK-10	Realgar	3.67	
CK-92C	Realgar	4.62	
C-T21	Pyrite	−3.14	
C-T22	Pyrite	−1.57	
C-T27	Pyrite	8.73	
C-T10	Pyrite	1.46	
C-T12	Pyrite	1.33	[13]
C-T4	Realgar	3.93	
C-T8	Stibnite	1.47	
C-T3	Stibnite	0.11	
C-T2	Stibnite	−0.45	
ckp13-1	Realgar	5.3	
ckp6-9	Realgar	1.3	This study
ckp8-6	Pyrite	1.2	

Table 4. S isotope data of the sulfides from the silver orebody.

Sample	$\delta^{34}\text{S}_{\text{V-CDT}}(\text{‰})$			Reference
	Pyrite	Sphalerite	Galena	
CK-94		2.7	2.4	
CK-95		4.6	4.1	
CK-156		1.7	2.1	
CK-157		2.4	3.2	[64]
CK-160		3.8	3.7	
CK-34	−2.3			
C-T13		7.39	4.04	
C-T15	4.77		0.09	[13]
L-1	6.41	3.15	5.61	
CH-15S	4.82			
CH-21S	−6.14			
CH-14S		4.2	0.07	[16]
CH-5S		5.75	1.91	
CH-11S	4.72	3.16	3.5	
CKZK2403-6(1)	4.89	4.76	2.28	
CKZK3209-2		3.27		
CKZK4401-1		4.07		
CKZK2403-4(1)		5.29		
CKZK3206-4(1)	4.95	3.34	1.24	[21]
CKZK3206-4(3)	4.99			
CKZK1001-3	1.59	3.38	2.33	
CKZK4401-3(1)		4.39	1.5	
ckp14-2		3.6		
ckp22-5	−2.7			
ckp34-1	−2.4			
ckp22-4	−8.7			This study
ckp5-5	−3.8			
ckp29-3		3.6		

The analytical results of the lead isotopes from the Au and Ag orebodies are listed in Table 5. Overall, the individual isotopic values of sulfides from the two orebodies fell within a narrow range. In the Au orebody, the  $^{206}\text{Pb}/^{204}\text{Pb}$  values of the pyrite were 18.477 to 20.356,  $^{207}\text{Pb}/^{204}\text{Pb}$  from 15.678 to 15.824, and  $^{208}\text{Pb}/^{204}\text{Pb}$  from 38.842 to 39.270. The corresponding values in the stibnite and realgar were 18.580–19.537, 15.672–15.750, and 38.700–39.032, respectively. In the Ag orebody, the pyrite showed  $^{206}\text{Pb}/^{204}\text{Pb}$  values varying from 18.596 to 18.871,  $^{207}\text{Pb}/^{204}\text{Pb}$  from 15.685 to 15.941, and  $^{208}\text{Pb}/^{204}\text{Pb}$  from 38.977 to 39.854. The corresponding values in the galena were 18.702 to 18.953, 15.682 to 15.951, and 38.911 to 39.804, respectively. The corresponding values in the sphalerite were 18.704 to 18.932, 15.715 to 15.936, and 39.099 to 39.698, respectively.

**Table 5.** Pb isotope data of the ores from the Changkeng–Fuwan Au–Ag deposit.

Orebody	Sample	Mineral	$^{206}\text{Pb}/^{204}\text{Pb}$	$^{207}\text{Pb}/^{204}\text{Pb}$	$^{208}\text{Pb}/^{204}\text{Pb}$	Reference	
Au orebody	CK-32	Pyrite	19.092	15.797	39.075	[16]	
	CK-38	Pyrite	18.832	15.728	39.002		
	CH-3S	Pyrite	18.737	15.736	39.177		
	CK-33	stibnite	18.58	15.672	38.7		
	CKZK-1	Pyrite	18.996	15.705	38.987	[22]	
	CK-28	Pyrite	18.945	15.73	39.035		
	CK-5	stibnite	19.14	15.727	38.914		
	CK-25	stibnite	18.883	15.706	39.032		
	CK-92C	Realgar	18.666	15.708	39.024		
	ckp13-1	Pyrite	18.706	15.767	39.124	This study	
	ckp8-6	Pyrite	18.477	15.678	38.842		
	Ag orebody	CK-156	Galena	18.845	15.902	39.69	[64]
		CK-160	Galena	18.834	15.848	39.657	
CK-157		Galena	18.851	15.873	39.658		
CK-95		Galena	18.891	15.914	39.786		
CK-94		Galena	18.82	15.848	39.579		
CH-15S		Pyrite	18.871	15.941	39.854		
CH-14S		Galena	18.702	15.687	39.015		
CH-5S		Galena	18.887	15.682	38.991		
CH-6S		Galena	18.825	15.86	39.561		
ZK2403-6		Galena	18.713	15.72	39.087	[22]	
ZK2403-6		Sphalerite	18.768	15.796	39.335		
ZK2403-6		Pyrite	18.667	15.685	38.997		
ZK3209-2		Sphalerite	18.72	15.725	39.119		
ZK4401-1		Sphalerite	18.704	15.715	39.118		
ZK2403-4		Sphalerite	18.932	15.936	39.698		
ZK3206-4		Galena	18.835	15.867	39.596		
ZK3206-4		Sphalerite	18.716	15.718	39.099		
ZK3206-4		Pyrite	18.772	15.787	39.33		
ZK1001-3		Galena	18.935	15.951	39.804		
ZK1001-3	Pyrite	18.596	15.746	39.095			
ZK4401-3	Galena	18.722	15.73	39.124			
ZK4401-3	Sphalerite	18.841	15.882	39.627			
ckp22-5	Pyrite	18.745	15.752	39.207	This study		
ckp29-3	Sphalerite	18.797	15.823	39.448			
ckp5-5	Pyrite	18.762	15.742	39.209			

### 5.6. He and Ar Isotopes

The He and Ar isotopic data of the Changkeng–Fuwan Au–Ag deposits are listed in Table 6. In the Au orebody, the  $^3\text{He}/^4\text{He}$  values varied from 2.46 to 2.50 Ra, where Ra ( $=1.4 \times 10^{-6}$ ) represents the atmospheric  $^3\text{He}/^4\text{He}$  values [66]. The  $^{40}\text{Ar}/^{36}\text{Ar}$  values of the two analyzed samples were 304.6 and 300.2, slightly higher than the atmospheric standard values (295.5) [67]. The  $^4\text{He}$  concentrations in the pyrite showed a variation

between 1.30 and 3.65 ( $10^{-8}$  cm<sup>3</sup> STP/g). The <sup>40</sup>Ar concentrations in the pyrite ranged from 2.77 to 22.20 ( $10^{-8}$  cm<sup>3</sup> STP/g). In the Ag orebody, the <sup>3</sup>He/<sup>4</sup>He values ranged from 1.41 to 5.70 Ra (average 3.88 Ra). The <sup>40</sup>Ar/<sup>36</sup>Ar values varied from 295.6 to 314.7 with a mean value of 300.9, higher than that of air (295.5). The <sup>4</sup>He concentrations ranged from 0.49 to 19.70 ( $10^{-8}$  cm<sup>3</sup> STP/g) with an average value of 6.20 ( $10^{-8}$  cm<sup>3</sup> STP/g), and those of <sup>40</sup>Ar varied from 2.35 to 30.00 ( $10^{-8}$  cm<sup>3</sup> STP/g) with a mean value of 9.29 ( $10^{-8}$  cm<sup>3</sup> STP/g).

**Table 6.** He and Ar isotopic data of the Changkeng–Fuwan Au–Ag deposit.

Sample	Mineral	<sup>3</sup> He	<sup>4</sup> He	<sup>40</sup> Ar	<sup>3</sup> He/ <sup>4</sup> He	R/Ra	<sup>40</sup> Ar/ <sup>36</sup> Ar	<sup>38</sup> Ar/ <sup>36</sup> Ar
ckp8-6	Pyrite, Au ore	$1.26 \times 10^{-13}$	$3.65 \times 10^{-8}$	$2.77 \times 10^{-8}$	$3.45 \times 10^{-6}$	2.46	304.6	0.182
ckp13-1	Pyrite, Au ore	$4.55 \times 10^{-14}$	$1.30 \times 10^{-8}$	$2.22 \times 10^{-7}$	$3.50 \times 10^{-6}$	2.5	300.2	0.179
ckp22-5	Pyrite, Ag ore	$3.90 \times 10^{-13}$	$1.97 \times 10^{-7}$	$3.00 \times 10^{-7}$	$1.98 \times 10^{-6}$	1.41	295.9	0.175
ckp33-23	Sphalerite, Ag ore	$3.69 \times 10^{-13}$	$6.75 \times 10^{-8}$	$3.60 \times 10^{-8}$	$5.47 \times 10^{-6}$	3.91	295.6	0.186
ckp36-4	Sphalerite, Ag ore	$3.95 \times 10^{-14}$	$4.94 \times 10^{-9}$	$5.50 \times 10^{-8}$	$7.99 \times 10^{-6}$	5.70	302.5	0.223
ckp19-2	Sphalerite, Ag ore	$6.52 \times 10^{-14}$	$8.70 \times 10^{-9}$	$2.35 \times 10^{-8}$	$7.49 \times 10^{-6}$	5.35	314.7	0.226
ckp28-23	Galena, Ag ore	$1.86 \times 10^{-13}$	$3.20 \times 10^{-8}$	$1.16 \times 10^{-7}$	$5.81 \times 10^{-6}$	4.15	298.1	0.198
ckp34-12	Pyrite, Ag ore	$2.49 \times 10^{-13}$	$6.45 \times 10^{-8}$	$2.66 \times 10^{-8}$	$3.86 \times 10^{-6}$	2.76	298.7	0.218

### 5.7. C–O Isotopes

The C and O isotope data in the Changkeng–Fuwan Au–Ag deposit are listed in Table 7. The  $\delta^{13}\text{C}_{\text{V-PDB}}$  and  $\delta^{18}\text{O}_{\text{V-PDB}}$  values in the Au orebody varied from  $-0.7$  to  $1.3\text{‰}$  (average  $0.6\text{‰}$ ), and  $-17.2$  to  $-11.2\text{‰}$  (average  $-13.3\text{‰}$ ), respectively. The corresponding values in the Ag orebody were  $-1.2$  to  $1.5\text{‰}$  (average  $0.03\text{‰}$ ) and  $-18.4$  to  $-13.2\text{‰}$  (average  $-16.6\text{‰}$ ), respectively. The calculated  $\delta^{18}\text{O}_{\text{V-SMOW}}$  values in the Au orebody showed a variation ranging from  $13.2$  to  $18.9\text{‰}$  (mean  $17.2\text{‰}$ ). The corresponding values in the Ag orebody ranged from  $11.9$  to  $17.3\text{‰}$  (mean  $13.8\text{‰}$ ).

**Table 7.** C and O isotopic data of the Changkeng–Fuwan Au–Ag deposit.

Sample	Mineral	$\delta^{13}\text{C}_{\text{V-PDB}}\text{‰}$	$\delta^{18}\text{O}_{\text{V-PDB}}\text{‰}$	$\delta^{18}\text{O}_{\text{V-SMOW}}\text{‰}$
ckp33-1	Calcite, the late stage of Au ore	$-0.7$	$-11.6$	18.9
ckp33-6		$+1.3$	$-11.2$	19.4
ckp8-6		$+1.2$	$-17.2$	13.2
ckp10-4	Calcite, the late stage of Ag ore	$-0.1$	$-17.6$	12.8
ckp16-2		$-1.2$	$-13.2$	17.3
ckp24-2		$+1.0$	$-18.4$	11.9
ckp25-1		$-0.3$	$-17.1$	13.2
ckp26-3		$-0.7$	$-18.4$	11.9
ckp34-9		$+1.5$	$-15$	15.4

## 6. Discussion

### 6.1. Fluid Evolution

Fluid inclusions can provide insights into the metallogenic processes of hydrothermal systems [54,68,69]. The evolution of the fluids for the Changkeng–Fuwan Au–Ag deposit can be reconstructed by petrographic, microthermometric, and laser Raman spectroscopy data of the FIs, which indicate that the ore-forming fluid in the Au and Ag mineralizations showed similarity in their chemical and physical properties. As described earlier, the type I inclusions dominated in the Au and Ag mineralizations. Laser Raman spectroscopy data indicated that the H<sub>2</sub>O dominated the vapor and liquid phases with no other volatiles detected. In the early stage, the ore-forming fluid was represented by medium-low temperature and medium-low salinity, which belonged to the NaCl–H<sub>2</sub>O system (Figures 8 and 9, Table 2). In the late stage, the ore-forming fluid had a low temperature and low salinity and turned into an H<sub>2</sub>O–NaCl system (Figures 8 and 9, Table 2). Low-salinity fluids can be generated by the mixing of meteoric water with magmatic fluids [70]. These features,

combined with the results of the H and O isotopes (Figure 11), indicate that the primary ore-forming fluid probably mixed with meteoric water infiltrating downward along the fractures. As the mineralization progressed, meteoric water was involved (Figure 11), which led to a temperature and salinity decrease in the ore fluid.

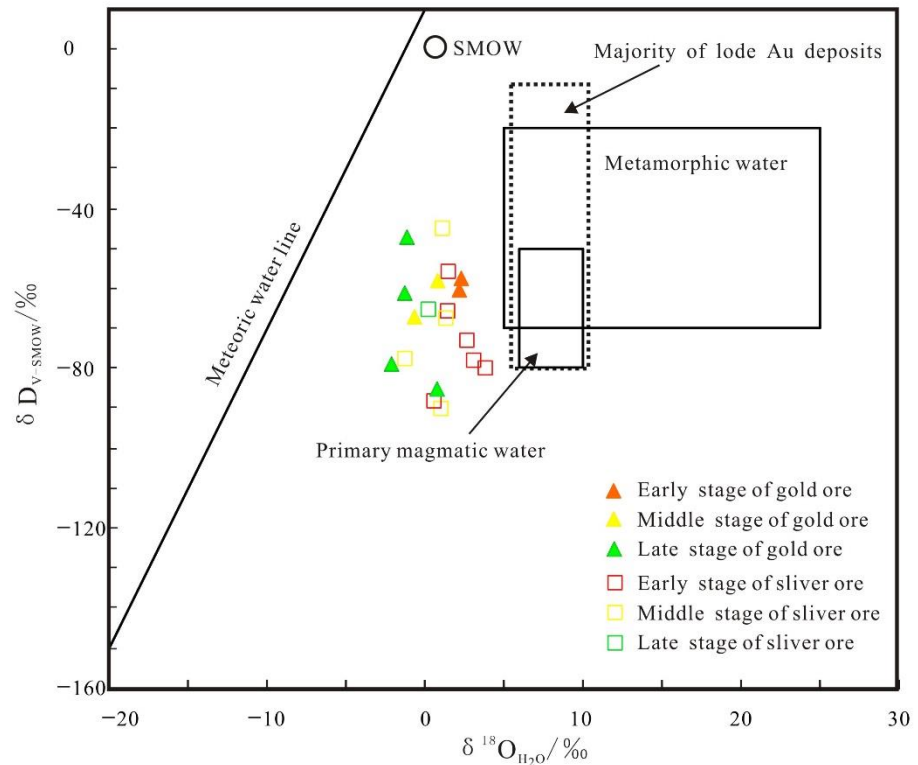


Figure 11. Plot of  $\delta D$  vs.  $\delta^{18}O_{H_2O}$  for the Changkeng–Fuwan Au-Ag deposit (from [70]).

The Th of the FIs in the Au mineralization ranged from 158 to 282 °C. The corresponding values in the Ag mineralization were between 146 and 289 °C. The salinities of the FIs were 0.35–9.88 wt.% and 0.18–11.7 wt.% NaCl equivalent, respectively. The Th and salinity diagrams [71] show that the three fluid groups depicted an obvious descending trend (Figure 12). This trend indicates a product of the gradual mixing of magmatic fluid with meteoric water [72].

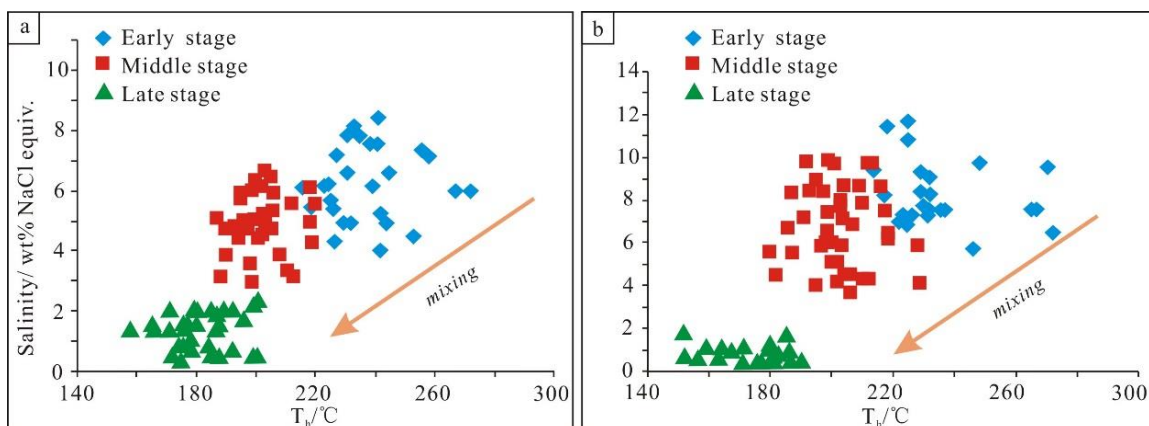


Figure 12. Th versus salinity of the fluid inclusions in different stages of the Changkeng–Fuwan Au (a)-Ag (b) deposit.

## 6.2. Source of Ore-Forming Fluids

H and O isotopic analyses play a critical role in tracing the origin and evolution history of fluids [73–77]. The  $\delta D$ - $\delta^{18}O$  isotopic diagram shows that the H and O isotopic data of the Au and Ag orebodies had a similar distribution (Figure 11). This implies that the sources of the ore-forming fluids for the Au and Ag orebodies were similar. The H and O isotopic results from the Au and Ag orebodies fell between the magmatic water region and the meteoric water line (Figure 11), and most data plots were close to the primary magmatic region. This suggests that the magmatic component contributed more than the meteoric water. The fluids of the deposit may be partly derived from magmatic fluid, and meteoric water was involved during the mineralization. It was also consistent with the late stage fluids with low temperature and salinity caused by a meteoric water source.

He and Ar isotopic analyses also play a critical role in tracing the origin of ore-forming fluids [66,78]. Generally, the source of the He-Ar isotopes of the fluids were as follows: (1) air-saturated meteoric water (ASW); (2) mantle-derived fluids (MDF); and (3) crust-derived fluids (CDF) [66,79–83]. The ASW was characterized by  ${}^3\text{He}/{}^4\text{He} = 1.4 \times 10^{-6}$  and  ${}^{40}\text{Ar}/{}^{36}\text{Ar} = 295.5$ . The corresponding values in the MDF were 6–9 Ra (Ra =  ${}^3\text{He}/{}^4\text{He}$ ) and 40,000, respectively. The corresponding values in the CDF were 0.01–0.05 Ra and  $>295.5$ , respectively.

The values of the  ${}^3\text{He}/{}^4\text{He}$  in the FIs from the Au and Ag orebodies varied from 2.46 to 2.50 Ra and 1.41 to 5.70 Ra, respectively. The values were lower than the values of the mantle (6–9 Ra) but much higher than the values of the crust (0.01–0.05 Ra). In the  ${}^3\text{He}$ - ${}^4\text{He}$  diagram (Figure 13a), the value of  ${}^3\text{He}/{}^4\text{He}$  in the FIs from the Au and Ag orebodies had a similar distribution, and all data were plotted between the crustal and mantle helium isotopic values. This indicates that the ore-forming fluids of the deposit may be a mixture of the MDF and CDF. The percentage of the MDF can be calculated by the equation from [63]. The calculated results ranged from 17.85% to 72.59% (average 44.84%), reflecting that the ore-forming fluids of the deposit may mainly derive from the MDF with the addition of the CDF. In addition, the values of  ${}^{40}\text{Ar}/{}^{36}\text{Ar}$  varied from 295.6 to 314.7, with a mean value of 300.9, which was also slightly higher than that of air (295.5). The  ${}^{40}\text{Ar}/{}^{36}\text{Ar}$  values of the Au and Ag orebodies also showed a similar distribution in the R/Ra- ${}^{40}\text{Ar}/{}^{36}\text{Ar}$  diagram (Figure 13b). All data fell between the MDF and ASW values, which revealed that the fluids were formed by mixing meteoric water and mantle-derived fluids. Zeng et al. (2007) [84] proposed that the fluid of a magmatic source is characterized by high  ${}^3\text{He}/{}^4\text{He}$  and  ${}^{40}\text{Ar}/{}^{36}\text{Ar}$  values, and the fluid of a meteoric source has low  ${}^3\text{He}/{}^4\text{He}$  and  ${}^{40}\text{Ar}/{}^{36}\text{Ar}$  values. The He and Ar data suggest that the fluids of the deposit may be a mixture of a magmatic source and a meteoric source.

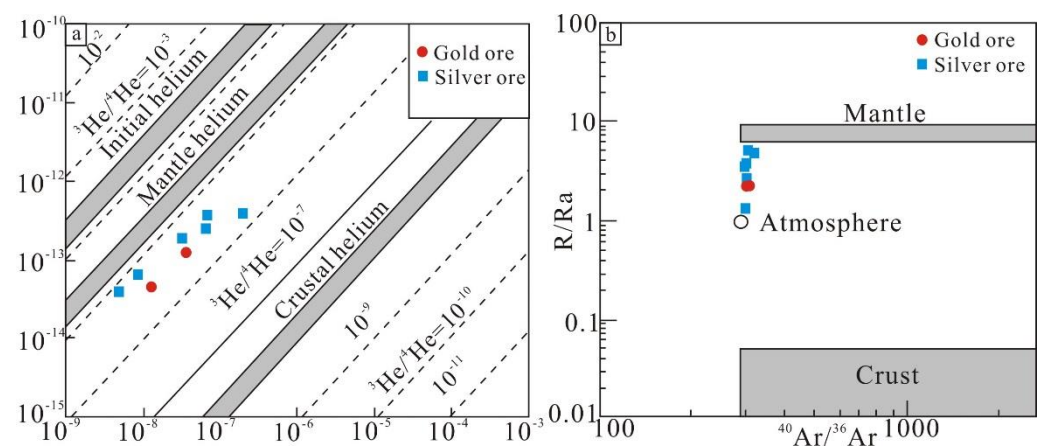


**Figure 13.** He isotopic data (a) and the  ${}^{40}\text{Ar}/{}^{36}\text{Ar}$ -R/Ra diagram (b) of the Changkeng-Fuwan Au-Ag deposit (after [85]).

The C and O isotopic analyses are often used to trace the origin of the carbon in ore-forming fluids [86–88]. The carbon in the fluids included three sources: (1) the upper mantle, (2) marine carbonate, and (3) sedimentary organic matter carbonate [85]. The  $\delta^{13}\text{C}_{\text{V-PDB}}$  values of calcite from the Au and Ag orebody ranged from  $-0.7$  to  $1.3\text{‰}$  and  $-1.2$  to  $1.5\text{‰}$ , respectively, which were slightly higher than the mantle source ( $-8$  to  $-2\text{‰}$ ) [89]. The  $\delta^{18}\text{O}_{\text{V-SMOW}}$  values of calcite ranged from  $13.2$  to  $18.9\text{‰}$  and  $11.9$  to  $17.3\text{‰}$ , respectively, which were obviously higher than the mantle source ( $6.5$  to  $9.5\text{‰}$ ) [89]. The C and O isotopic data of calcite from the Au and Ag orebodies had a similar distribution (Figure 12). All the data were plotted between the magmatic field [85] and marine carbonate field [90]. Moreover, the samples showed a horizontal zonation pattern between  $\delta^{13}\text{C}_{\text{V-PDB}}$  and  $\delta^{18}\text{O}_{\text{V-SMOW}}$  (Figure 14). Therefore, the carbon of fluids may derive from a magmatic source [91]. In summary, we conclude that the source of the fluids in the Changkeng–Fuwan deposit were a mixture of magmatic fluid and meteoric water.

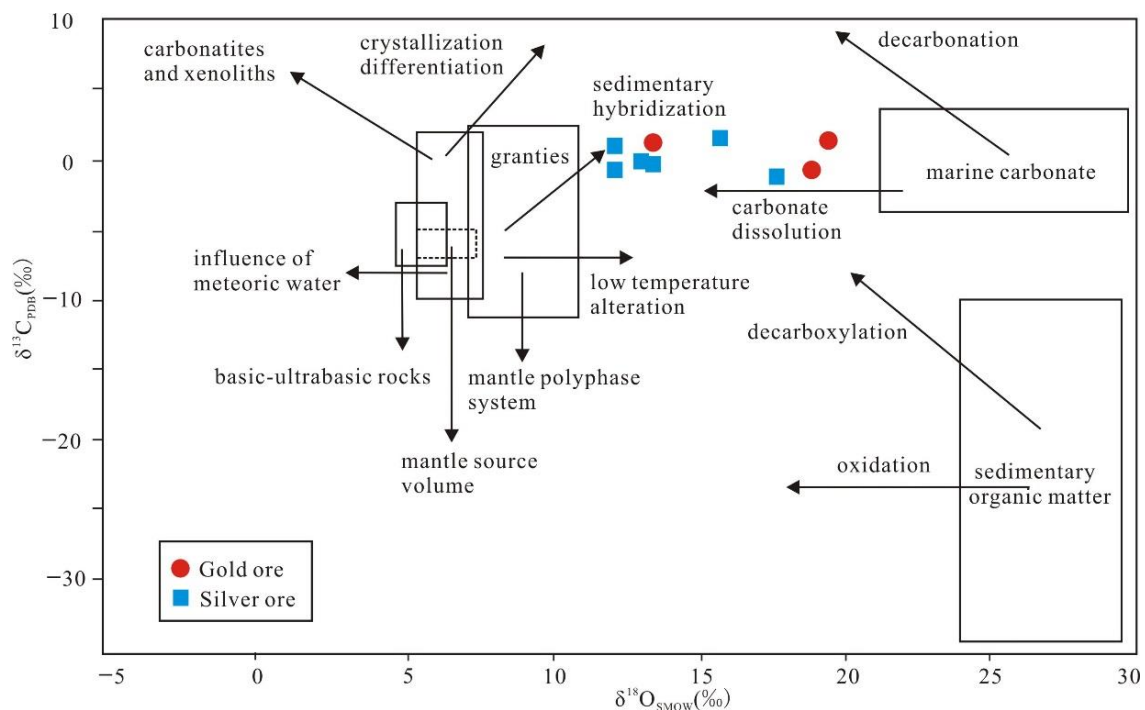


**Figure 14.** Plot of  $\delta^{13}\text{C}_{\text{PDB}}$  vs.  $\delta^{18}\text{O}_{\text{SMOW}}$  for the Changkeng–Fuwan Au–Ag deposit (from [92]).

### 6.3. Source of Ore-Forming Metals

S isotopic analyses can effectively trace the origin of the metals in ore-forming fluids [81–83,93–98]. Studies on the sulfides related to the Au and Ag mineralizations are helpful to understand the source of the Au and Ag in ore-forming fluids [99–101], due to the lack of sulfate minerals in the Changkeng–Fuwan deposit. Thus, the total S isotopic compositions of the ore-forming fluids can be represented by the  $\delta^{34}\text{S}$  values of sulfides [102]. The  $\delta^{34}\text{S}$  values of the sulfides from the Au and Ag orebodies in this study and previous studies ranged from  $-5.8$  to  $+8.73\text{‰}$  (mean  $-0.84\text{‰}$ ; Table 3; Figure 15a) and  $-8.7$  to  $+7.39\text{‰}$  (mean  $2.58\text{‰}$ ; Table 4; Figure 15b), respectively, which were close to the value of magmatic sulfides ( $0 \pm 5\text{‰}$ ; [92]). This suggests that the sulfur of the Changkeng–Fuwan deposit mainly came from magmatic sulfur [103–105].

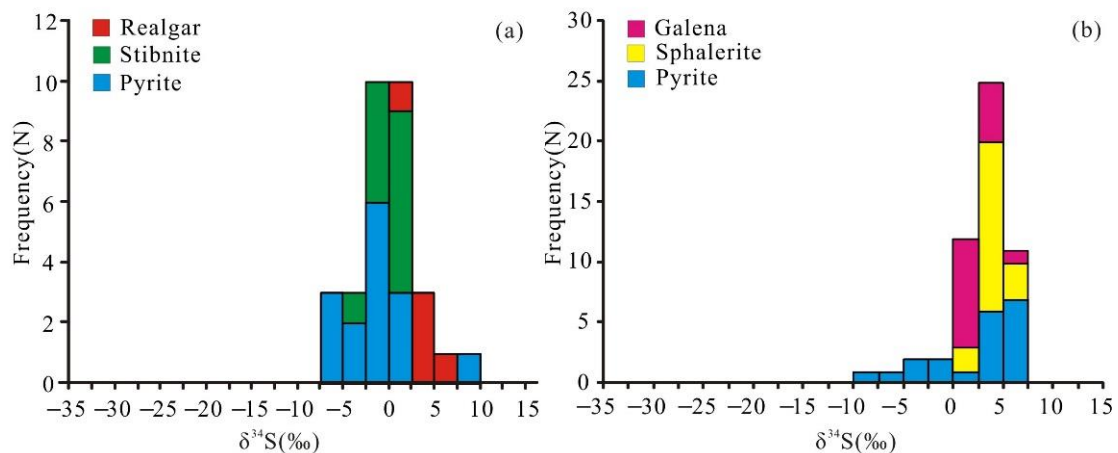


**Figure 15.** Histogram of the S isotope data for the Changkeng–Fuwan Au (a)–Ag (b) deposit.

The Pb isotopic data can provide indicators about the origin of metal and the tectonic environment of the mineralization [106–108]. We analyzed the Pb isotopes of the Au and Ag orebodies, combined with previously published Pb isotopic data. The Pb isotopic data from the Au and Ag orebodies fell within a narrow range (Table 5). The diagram of  $^{207}\text{Pb}/^{204}\text{Pb}$  versus  $^{206}\text{Pb}/^{204}\text{Pb}$  (Figure 16) indicates that all the Pb isotopic data were plotted above or near the upper crust curve, which was consistent with the previous studies. Zhu (1998) [109] proposed that the ratios of  $^{207}\text{Pb}/^{204}\text{Pb}$  and  $^{208}\text{Pb}/^{204}\text{Pb}$  can also reveal the source of the metal, while  $^{206}\text{Pb}/^{204}\text{Pb}$  is sensitive to the time of mineralization. Comparison of data from different rock types can determine the ore formation mechanism. The  $\Delta\beta$ – $\Delta\gamma$  diagram can reflect the tectonic environment and source of the metal, which is not influenced by the time factor. It can more effectively trace the origin of metals than global patterns of evolution. The values of  $\Delta\beta$  and  $\Delta\gamma$  can be calculated by the equation of Zhu (1998) [109] and Wei (2020) [110]. The diagram of  $\Delta\beta$ – $\Delta\gamma$  (Figure 17) further shows that the Pb isotopic data were distributed in the upper crust field or near fields between the upper crust and the mantle. Therefore, the source of the Pb in the Changkeng–Fuwan deposit was predominantly from the upper crust, with a minor contribution of mantle-derived Pb.

Hence, we conclude that the primary source of the metals in the Changkeng–Fuwan deposit may be magmatic fluids.

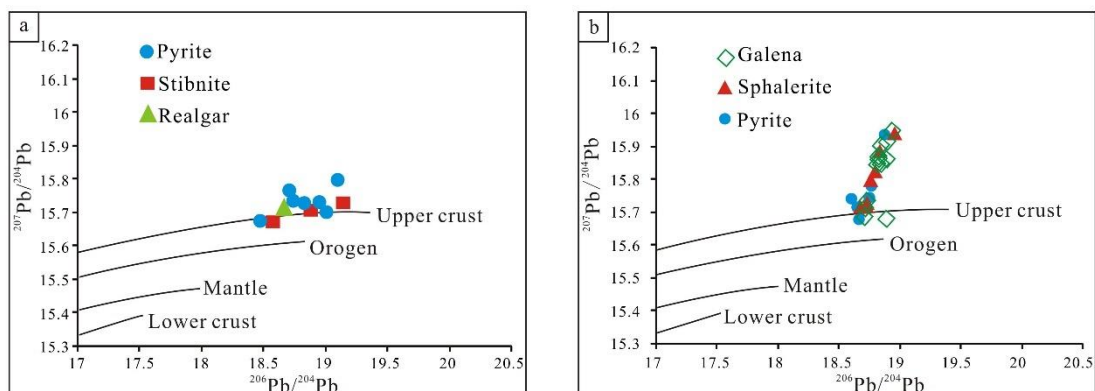


**Figure 16.** Plot of the Pb isotopic data for the sulfides from the Changkeng–Fuwan Au (a)–Ag (b) deposit; the evolution curves of the upper crust, lower crust, mantle, and orogen are from [111].

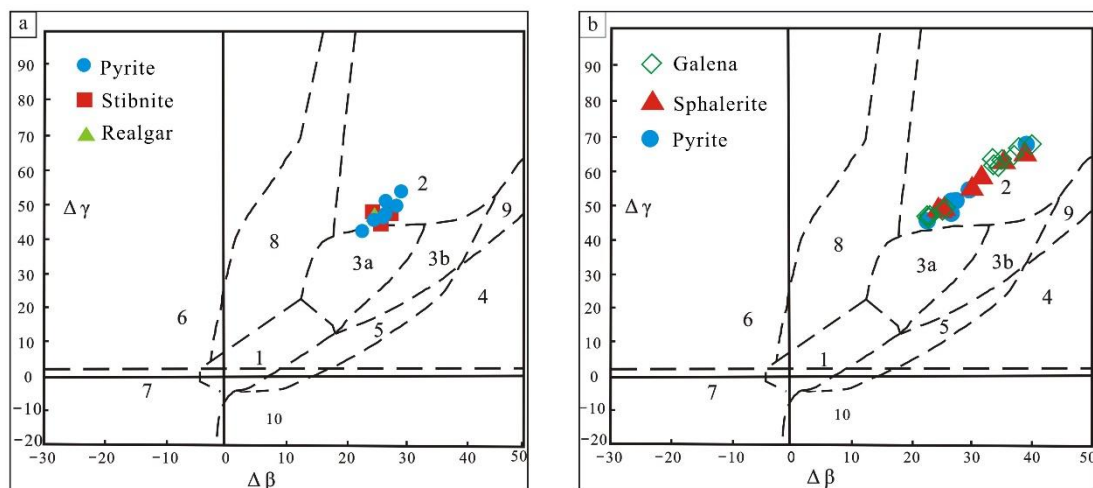


**Figure 17.** Plot of  $\Delta\beta$  vs.  $\Delta\gamma$  for the Changkeng–Fuwan Au (a)–Ag (b) deposit (base map is from [109]). The Pb sources are: (1) mantle; (2) upper crust; (3) (3a, magmatism; 3b, sedimentation); (4) chemical sedimentation; (5) hydrothermal sedimentation; (6) mesometamorphism; (7) deep metamorphic lower crust; (8) orogenic belt; (9) ancient shale crust; and (10) retrograde metamorphism.

#### 6.4. Mineralization Zonation

Our new data from the FIs and isotopic analyses showed that the origin and evolution of the ore-forming fluids and metals of the Au and Ag mineralizations were similar. Therefore, the Au and Ag mineralizations were formed in the same metallogenic system. However, the gold and silver orebodies were independent of one another, with the characteristics of “north gold and south silver” in the plane and “upper gold and lower silver” in the section. Xue et al. [112] suggested that there were two main types of gold deposits in China according to the study of 450 representative gold deposits. One is characterized as Au and Ag associated, with low Pb and Zn contents; the other is Au, As, and Sb associated, with low Ag contents. The statistical results of the mineralization element contents of 125 gold and silver ores samples in the boreholes showed that the Au and Ag orebodies were not completely separated but associated with each other. In particular, in the contact area of the Au and Ag orebodies in the central part, both the contents of the Au and Ag in the same spatial position were close to or above the cut-off grade. The elements of Au (As, Sb)–Au (Ag)–Ag (Au, Pb, Zn, Cu) were zoned with depth. Considering the geochemical characteristics of the elements, we propose that the reason for the mineralization zonation of the Au and Ag orebodies are as follows: Au is a variable element with three forms,  $\text{Au}^+$ ,  $\text{Au}^{3+}$ , and  $\text{Au}^0$ .  $\text{Au}^+$  is a strong alkaline cation, and its ionic potential is similar to that of  $\text{Cu}^+$  and  $\text{Ag}^+$ .  $\text{Au}^{3+}$  is a transition ion, and its ionic potential is similar to that of  $\text{Sb}^{3+}$  and  $\text{As}^{3+}$  [112–114]. Au migrates mainly in the form of  $\text{Au}^+$  at depth and is associated with  $\text{Ag}^+$ . The ionic potential of  $\text{Ag}^+$  and  $\text{Au}^+$  is as follows:  $\text{Ag}^+$  0.79 and  $\text{Au}^+$  0.73. Generally, if the coordination anions remain unchanged, the greater the ionic potential of the cations in the complex, the more stable the complex [115,116]. Thus, it presents lower silver (associated gold).  $\text{Au}^+$  is oxidized to  $\text{Au}^{3+}$  in the shallow to near-surface, which is associated with  $\text{As}^{3+}$  and  $\text{Sb}^{3+}$ , and presents upper gold (associated silver). In addition, the Au, As, and Sb elements can migrate in the gas phase; so,  $\text{Au}^{3+}$ ,  $\text{As}^{3+}$ , and  $\text{Sb}^{3+}$  can occur far away from the top of the metallogenic rock mass.

#### 6.5. Ore Deposition Mechanism and Genesis

Usually, the metals of the ore-forming fluid exist in the form of Cl- and HS-aqueous complexes, and temperature plays a critical role in the stability of the metal complexes [117–119]. A certain degree of cooling of the fluid will lead to the precipitation of the base metals. The ore-forming fluids of the Au and Ag mineralizations belong to the NaCl– $\text{H}_2\text{O}$  system with low-medium temperatures and low-medium salinities. The data of the FIs in the Au and

Ag mineralizations from the early stage to the late stage indicate that the temperature and salinity of the ore-forming fluids decreased continuously. It shows an integration of both mixing and cooling processes. Moreover, the H, O, He, and Ar isotopic data implied that the fluids of the deposit were formed by mixing meteoric and magmatic fluids. These FI and stable data demonstrate a simple cooling trend and mixing with meteoric waters during the evolution of the fluid [120–123]. Meanwhile, the data of the FIs from the middle-stage and late-stage with relatively lower salinity and lower temperature fail to provide any evidence for boiling. In summary, it is considered that fluid mixing ought to be the main mechanism for the deposition of Au and Ag.

Many researchers have proposed hypotheses for the genesis of the Changkeng–Fuwan Au–Ag deposit [14–17]. At present, its genesis remains controversial. There are two main views to interpret its genesis: (1) epithermal deposit [15] and (2) magmatic hydrothermal deposit [17]. The Changkeng–Fuwan Au–Ag deposit has unique geological features, which differ greatly from a typical epithermal Au–Ag deposit. Meanwhile, the hydrothermal alteration and mineral assemblage of the deposit are inconsistent with the epithermal deposit [124,125]. Based on the new data in this study, we propose that the Changkeng–Fuwan Au–Ag deposit might be classified as a far-source low-temperature magmatic hydrothermal deposit [112,113]. The detailed reasons for the classification are as follows:

(1) The orebodies of the far-source low-temperature magmatic hydrothermal deposit are hosted in a clastic rock–carbonate–siliceous rock formation and are mainly controlled by faults. The orebodies in the Changkeng–Fuwan Au–Ag deposit occur within Zimenqiao Formation siliceous rocks and limestone and are mainly controlled by faults.

(2) The ore minerals of the Changkeng–Fuwan Au–Ag deposit predominantly consist of pyrite, galena, sphalerite, and silver-bearing minerals, with minor chalcopyrite; while the gangue minerals are mostly quartz, sericite, and calcite, with accessory realgar and fluorite. The hydrothermal alteration of both the Au and Ag mineralizations is similar. The main alteration types consist of silicification, sericitization, sulfidation, and carbonatization. Among these, silicification and sulfidation are the most common types. The early stage of the deposit is characterized by silicification. The alteration and mineral assemblage of the Changkeng–Fuwan Au–Ag deposit are similar to a far-source low temperature magmatic hydrothermal deposit.

(3) The type of FIs in a far-source low-temperature magmatic hydrothermal deposit is characterized by aqueous liquid FIs. The homogenization temperatures range from 140 to 300 °C. The types of FIs in the Changkeng–Fuwan Au–Ag deposit were two-phase liquid-rich inclusions and monophasic liquid inclusions. The ore-forming fluids of the Au and Ag mineralizations were generally characterized by low-medium temperatures and low-medium salinities and belong to a NaCl–H<sub>2</sub>O system.

(4) The C, H, O, He, and Ar isotopic data demonstrate that magmatic-derived fluid matters during mineralization. In addition, the S and Pb isotopic data show that the primary source of the metals in the Changkeng–Fuwan deposit may be a magma source.

(5) The orebodies of far-source low-temperature magmatic hydrothermal deposit are often far from the igneous intrusion. Although there are no exposures of igneous rocks at the surface in the mine district, related geophysical data showed that a concealed pluton underlay the Changkeng–Fuwan Au–Ag deposit. The concealed pluton may provide the most important mineral and heat sources for the Changkeng–Fuwan deposit.

Collectively, the geological setting, ore geology, hydrothermal alteration, and the characteristics of the fluid and stable isotopic data above attest that the Changkeng–Fuwan Au–Ag deposit belongs to a far-source low-temperature magmatic hydrothermal deposit.

## 7. Conclusions

(1) The Au and Ag mineralizations of the Changkeng–Fuwan deposit are the products of the same metallogenic system, and three metallogenic stages were identified: a pyrite–quartz–sericite stage (early), a polymetallic sulfide stage (middle), and a quartz–calcite stage (late).

(2) The ore minerals of the Changkeng–Fuwan Au–Ag deposit predominantly consisted of pyrite, galena, sphalerite, and silver-bearing minerals, with minor chalcopyrite; while the gangue minerals were mostly quartz, sericite, and calcite, with accessory realgar and fluorite.

(3) Two types of FIs were recognized: two-phase liquid-rich inclusions (type I) and monophasic liquid inclusions (type II).

(4) The ore-forming fluids of the Au and Ag mineralizations were generally presented by low-medium temperatures and low-medium salinities and belong to a NaCl–H<sub>2</sub>O system. Fluid mixing ought to be the main mechanism for the deposition of Au and Ag.

(5) The isotopic data (C, H, O, He, Ar, S, and Pb) showed that the source of fluids in the Changkeng–Fuwan deposit was a mixture of magmatic fluid and meteoric water, and the primary source of the metals may be magmatic fluids.

(6) Integration of the regional geology, ore geology, hydrothermal alteration, fluid inclusion, and the isotope study indicate that the Changkeng–Fuwan Au–Ag deposit belongs to a far-source low temperature magmatic hydrothermal deposit.

**Author Contributions:** G.S., J.X. and X.Z. conceived and designed the ideas; G.S., J.X., Z.P., W.T. and S.Z. collected and analyzed the data; G.S. wrote the manuscript; J.X., X.Z., X.W., F.Y. and G.J. revised and edited the manuscript. All authors have read and agreed to the published version of the manuscript.

**Funding:** This study was financially supported by the Geological Survey Projects of China Geological Survey (No. DD20190570; No. DD20221692).

**Data Availability Statement:** Not applicable.

**Acknowledgments:** We thank Kunfeng Qiu (China University of Geosciences Beijing) for his constructive reviews and suggestions. We also thank the staff of the Mingke Mining Company for their assistance in the field. Tianzhu Ye, Hui Chen, Yanwen Zhang, Hongxiang Jia, and Lujun Lin from the China Geological Survey are also thanked for their constructive suggestions during this study. In addition, we appreciate the kind help from Huiyan Zhu and He Zhang (China University of Geosciences Beijing) and Mu Liu, Hanbin Liu, and Guangxi Ou (Beijing Research Institute of Uranium Geology) within the laboratory.

**Conflicts of Interest:** The authors declare no conflict of interest.

## References

1. Li, H.; Kong, H.; Zhou, Z.K.; Wu, Q.H.; Xi, X.S.; Gabo-Ratio, J.A.S. Ore-forming metal sources of the Jurassic Cu–Pb–Zn mineralization in the Qin–Hang ore belt, South China: Constraints from S–Pb isotopes. *Geochemistry* **2019**, *79*, 280–306. [[CrossRef](#)]
2. Wu, S.; Mao, J.; Xie, G.; Geng, J.; Xiong, B. Geology, geochronology, and Hf isotope geochemistry of the Longtougang skarn and hydrothermal vein Cu–Zn deposit, North Wuyi area, southeastern China. *Ore Geol. Rev.* **2015**, *70*, 136–150. [[CrossRef](#)]
3. Ni, P.; Wang, G.G.; Cai, Y.T.; Zhu, X.T.; Yuan, H.X.; Huang, B.; Ding, J.Y.; Chen, H. Genesis of the late jurassic shizitou Mo deposit, South China: Evidences from fluid inclusion, H–O isotope and Re–Os geochronology. *Ore Geol. Rev.* **2017**, *81*, 871–883. [[CrossRef](#)]
4. Zhou, Y.Z.; Zeng, C.Y.; Li, H.Z.; An, Y.F.; Lu, W.C.; Yang, Z.J.; Shen, W.J. Geological evolution and ore-prospecting targets in southern segment of Qinzhou Bay–Hangzhou Bay juncture orogenic belt, southern China. *Geol. Bull. China* **2012**, *31*, 486–491. (In Chinese with English Abstract).
5. Wang, Y.J.; Fan, W.M.; Zhang, G.W.; Zhang, Y.H. Phanerozoic tectonics of the South China Block: Key observations and controversies. *Gondwana Res.* **2013**, *23*, 1273–1305. [[CrossRef](#)]
6. Zheng, Y.; Zhou, Y.Z.; Wang, Y.J.; Shen, W.J.; Yang, Z.J.; Li, X.Y. A fluid inclusion study of the Hetai goldfield in the Qinzhou Bay–Hangzhou Bay metallogenic belt, South China. *Ore Geol. Rev.* **2016**, *73*, 346–353. [[CrossRef](#)]
7. Jiao, Q.Q.; Deng, T.; Wang, L.X.; Xu, D.R.; Chi, G.X.; Chen, G.W.; Zou, S.H. Geochronological and mineralogical constraints on mineralization of the Hetai goldfield in Guangdong Province, South China. *Ore Geol. Rev.* **2017**, *88*, 655–673. [[CrossRef](#)]
8. Jiao, Q.Q.; Wang, L.X.; Deng, T.; Xu, D.R.; Chen, G.W.; Yu, D.S.; Ye, T.W.; Gao, Y.W. Origin of the ore-forming fluids and metals of the Hetai goldfield in Guangdong Province of South China: Constraints from C–H–O–S–Pb–He–Ar isotopes. *Ore Geol. Rev.* **2017**, *88*, 674–689. [[CrossRef](#)]
9. Wang, Y.; Fan, W.; Zhao, G.; Ji, S.; Peng, T. Zircon U–Pb geochronology of gneissic rocks in the Yunkai massif and its implications on the Caledonian event in the South China Block. *Gondwana Res.* **2007**, *12*, 404–416. [[CrossRef](#)]

10. Mao, J.W.; Chen, M.H.; Yuan, S.D.; Guo, C.L. Geological characteristics of the Qinhang (or Shihang) metallogenic belt in South China and spatial-temporal distribution regularity of mineral deposit. *Acta Geol. Sin.* **2011**, *85*, 636–658. (In Chinese with English Abstract)
11. Wang, C.H.; Zhang, C.Q.; Wang, Y.L.; Qiu, X.P. Chronological research of the Hetai gold mine in Gaoyao county, Guangdong Province. *Geotecton. Metallog.* **2012**, *36*, 427–433. (In Chinese with English Abstract)
12. Wang, L.; Xu, D.M.; Zhang, K.; Hu, J.; Xiao, G.M.; Xu, J.Y. Geological and geochemical characteristics and metallogenic age of Huangnikeng gold deposit in western Guangdong Province. *Miner. Depos.* **2017**, *36*, 317–329. (In Chinese with English Abstract)
13. Du, J.E.; Ma, C.H.; Wei, L. Geochemistry of Changkeng gold-silver deposit, Guangdong province. *Guangdong Geology* **1996**, *11*, 49–59. (In Chinese with English Abstract)
14. Mao, X.D.; Liu, Y.H. Metallogenic model of Changkeng gold and silver deposit in Guangdong Province. *Geol. Sci. Technol. Inf.* **2004**, *23*, 82–86. (In Chinese with English Abstract)
15. Liang, H.Y.; Xia, P.; Wang, X.Z.; Cheng, J.P.; Zhao, Z.H.; Liu, C.Q. Geology and geochemistry of the adjacent Changkeng gold and Fuwan silver deposit, Guangdong Province, South China. *Ore Geol. Rev.* **2007**, *31*, 304–318. [\[CrossRef\]](#)
16. Zhang, S.; Li, T.J.; Wang, L.K. Geochemistry and genesis of the Changkeng large-superlarge gold-silver deposit, Guangdong province. *Miner. Depos.* **1998**, *17*, 125–134. (In Chinese with English Abstract)
17. Zhuang, W.M.; Chen, G.N.; Lin, X.M.; Peng, Z.L.; Ma, H.M. Composition of oxygen isotopes and discussion on the formation of Changkeng Au-Ag deposit, Guangdong province. *J. Jilin Univ.* **2006**, *36*, 521–526. (In Chinese with English Abstract)
18. Mao, X.D.; Wu, W.H.; Huang, S.J. Ore types mineral assemblage of the Changkeng Au-Ag deposit, Guangdong, south China. *J. Chengdu Univ. Technol.* **2007**, *34*, 7–14. (In Chinese with English Abstract)
19. Zhang, W.H.; Lu, W.J.; Jiao, Y.Q.; Li, S.T. Composition and source study of ore-forming fluid in Changkeng gold-silver deposits, Guangdong province, China. *Acta Petrol. Sin.* **2000**, *16*, 521–527. (In Chinese with English Abstract)
20. Mao, X.D.; Huang, S.J.; Liu, Y.H. Geochemical characters and significance of the fluid inclusions from the Changkeng-Fuwan gold-silver deposit, Guangdong province. *J. Chengdu Univ. Technol.* **2003**, *30*, 111–119. (In Chinese with English Abstract)
21. Mao, X.D.; Huang, S.J. Characteristics of sulfur isotopes and its significance in Changkeng-Fuwan gold and silver deposit, Guangdong Province. *Geol. Miner. Resour. South China* **2002**, *1*, 17–22. (In Chinese with English Abstract)
22. Mao, X.D.; Huang, S.J. Characteristics and significance of lead isotopes of ores from the Changkeng-Fuwan gold-silver deposit, Guangdong Province. *Geol. Miner. Resour. South China* **2003**, *1*, 27–32. (In Chinese with English Abstract)
23. Liang, H.Y.; Wang, X.Z.; Cheng, J.P.; Xia, P.; Zhang, H.; Shan, Q. Rb-Sr dating and genesis of Changkeng-Fuwan superlarge silver deposit in west Guangdong. *Sci. Geol. Sin.* **2000**, *35*, 47–54. (In Chinese with English Abstract)
24. Mao, X.D.; Huang, S.J.; Liu, Y.H. The metallogenic epoch of the Changkeng-Fuwan Au-Ag deposit in Guangdong Province. *Prog. Nat. Sci.* **2003**, *13*, 95–98. (In Chinese with English Abstract)
25. Sun, X.M.; Chen, B.H. Hot spring genesis of the Changkeng gold-silver deposit in Guangdong province and its geological significance. *Acta Sci. Nat. Univ. Sunyatseni* **1995**, *34*, 131–133. (In Chinese with English Abstract)
26. Deng, J.; Wang, Q. Gold mineralization in China: Metallogenic provinces, deposit types and tectonic framework. *Gondwana Res.* **2016**, *36*, 219–274. [\[CrossRef\]](#)
27. Liu, Y.; Zhao, J.H.; Zhao, X.F.; Chen, H.M.; Luo, H.L. Texture and geochemistry of pyrite from the Gaoche gold deposit in South China: Implications of ore-forming processes. *Ore Geol. Rev.* **2020**, *126*, 103747. [\[CrossRef\]](#)
28. Wang, C.; Shao, Y.J.; Evans, N.J.; Li, H.; Zhou, H.D.; Huang, K.X.; Liu, Z.F.; Chen, Y.; Lai, C.; Liu, Q.Q. Genesis of Zixi gold deposit in Xuefengshan, Jiangnan Orogen (South China): Age, geology and isotopic constraints. *Ore Geol. Rev.* **2020**, *117*, 103301. [\[CrossRef\]](#)
29. Goldfarb, R.J.; Mao, J.W.; Qiu, K.F.; Goryachev, N. The great Yanshanian metallogenic event of eastern Asia: Consequences from one hundred million years of plate margin geodynamics. *Gondwana Res.* **2021**, *100*, 223–250. [\[CrossRef\]](#)
30. Hao, Z.M.; Xiao, Y.M.; Du, H.F.; Wang, Q.; Chang, J.; Shen, L.J.; Lin, L. Geochemistry of the Cunqian ore-bearing porphyry from the eastern Qin-Hang metallogenic belt and its implication for tectonic setting and mineralization. *Acta Petrol. Sin.* **2016**, *32*, 2069–2085.
31. Zhao, P.; Yuan, S.; Mao, J.; Santosh, M.; Li, C.; Hou, K. Geochronological and petrogeochemical constraints on the skarn deposits in Tongshanling ore district, southern Hunan Province: Implications for Jurassic Cu and W metallogenic events in South China. *Ore Geol. Rev.* **2016**, *78*, 120–137. [\[CrossRef\]](#)
32. Li, H.; Yonezu, K.; Watanabe, K.; Tindell, T. Fluid origin and migration of the Huangshaping W–Mo polymetallic deposit, South China: Geochemistry and <sup>40</sup>Ar/<sup>39</sup>Ar geochronology of hydrothermal K-feldspars. *Ore Geol. Rev.* **2017**, *86*, 117–129. [\[CrossRef\]](#)
33. Zhao, W.W.; Zhou, M.F.; Li, Y.H.M.; Zhao, Z.; Gao, J.F. Genetic types, mineralization styles, and geodynamic settings of Mesozoic tungsten deposits in South China. *J. Asian Earth Sci.* **2017**, *137*, 109–140. [\[CrossRef\]](#)
34. Zhao, P.L.; Yuan, S.D.; Yuan, Y.B. Geochemical characteristics of garnet in the Huangshaping polymetallic deposit, southern Hunan: Implications for the genesis of Cu and W–Sn mineralization. *Acta Petrol. Sin.* **2018**, *34*, 2581–2597.
35. Zhang, G.W.; Guo, A.L.; Wang, Y.J.; Li, S.Z.; Dong, Y.P.; Liu, S.F. Tectonics of South China continent and its implications. *Sci. China Earth Sci.* **2013**, *56*, 1804–1828. (In Chinese with English Abstract) [\[CrossRef\]](#)
36. Wang, L.X.; Zhao, Z.X.; Huang, Q.Y.; Xu, D.R.; Jiao, Q.Q.; Chen, G.W.; Cai, J.X.; Zou, S.H.; Teng, D.; Qiang, S. The genesis of gold deposit in the Hetai goldfield, South China: New constraints from geochronology, fluid inclusion, and multiple isotopic studies. *Geol. J.* **2019**, *55*, 2447–2472. [\[CrossRef\]](#)

37. Deng, J.; Qiu, K.F.; Wang, Q.F.; Goldfarb, R.J.; Yang, L.Q.; Zi, J.W.; Geng, J.Z.; Ma, Y. In situ dating of hydrothermal monazite and implications for the geodynamic controls on ore formation in the Jiaodong gold province, eastern China. *Econ. Geol.* **2020**, *115*, 671–685. [[CrossRef](#)]
38. Qiu, K.F.; Goldfarb, R.J.; Deng, J.; Yu, H.C.; Gou, Z.Y.; Ding, Z.J.; Wang, Z.K.; Li, D.P. Gold deposits of the Jiaodong Peninsula, eastern China. *SEG Spec. Publ.* **2020**, *23*, 753–773.
39. Deng, J.; Yang, L.Q.; Groves, D.I.; Zhang, L.; Qiu, K.F.; Wang, Q.F. An integrated mineral system model for the gold deposits of the giant Jiaodong province, eastern China. *Earth-Sci. Rev.* **2020**, *208*, 103274. [[CrossRef](#)]
40. Wan, Y.; Liu, D.; Wilde, S.A.; Cao, J.; Chen, B.; Dong, C. Evolution of the Yunkai Terrane, South China: Evidence from SHRIMP zircon U-Pb dating, geochemistry and Nd isotope. *J. Asian Earth Sci.* **2010**, *37*, 140–153. [[CrossRef](#)]
41. Ni, J.L.; Liu, J.L.; Wang, J.C.; Tang, X.L.; Wang, Z.; Li, Z.S.; Li, D.P. Ductile shear deformation and gold mineralization in the Hetai goldfield of the Yunkai Massif, South China Block. *Geol. J.* **2019**, *54*, 929–945. [[CrossRef](#)]
42. Jiao, Q.Q.; He, C.K.; Dong, Y.P.; Xu, D.R.; Chen, G.W.; Chen, C.; Shi, S.; Gao, Y.W. The petrogenetic links of Indosiniangranitoid and migmatite in the Hetai goldfield, Guangdong Province of South China and the tectonic implication. *Acta Petrol. Sin.* **2020**, *36*, 893–912.
43. Wang, Y.J.; Fan, W.M.; Cawood, P.A.; Ji, S.C.; Peng, T.P.; Chen, X.Y. Indosinian high-strain deformation for the Yunkai-dashan tectonic belt, South China: Kinematics and  $40\text{Ar}/^{39}\text{Ar}$  geochronological constraints. *Tectonics* **2007**, *26*, 229–247. [[CrossRef](#)]
44. Xu, X.B.; Zhang, Y.Q.; Jia, D.; Shu, L.S.; Wang, R.R. Early Mesozoic geotectonic processes in China. *Geol. China* **2009**, *36*, 573–593. (In Chinese with English Abstract)
45. Shu, L.S. An analysis of principal features of tectonic evolution in South China Block. *Geol. Bull. China* **2012**, *31*, 1035–1053. (In Chinese with English Abstract)
46. Cai, J.X. An early Jurassic dextral strike-slip system in southern South China and its tectonic significance. *J. Geodyn.* **2013**, *63*, 27–44. [[CrossRef](#)]
47. Peng, S.B.; Jin, Z.M.; Liu, Y.H.; Fu, J.M.; He, L.Q.; Cai, M.H. Petrochemistry, chronology and tectonic setting of strong peraluminous anatectic granitoids in Yunkai Orogenic Belt, Western Guangdong Province, China. *J. Earth Sci.* **2006**, *17*, 1–12. (In Chinese with English Abstract) [[CrossRef](#)]
48. Peng, S.B.; Wang, Y.; Wei, M.; Peng, T.; Liang, X. LA-ICPMS zircon U-Pb dating for three Indosinian Granitic plutons from Central Hunan and Western Guangdong Provinces and its petrogenetic implications. *Acta Geol. Sin.* **2006**, *80*, 660–669. (In Chinese with English Abstract)
49. Zhai, W.; Yuan, G.; Li, Z.L.; Huang, D. U-Pb isotope age of zircons in gold-bearing quartz veins from the Hetai gold deposit, Western Guangdong, China: Constraints on the timing of gold metallogenesis. *Geol. Rev.* **2005**, *51*, 340–346. (In Chinese with English Abstract)
50. Cai, M.; Zhan, M.; Peng, S.; Meng, X.; Liu, G. Study of Mesozoic metallogenic geological setting and dynamic mechanism in Yunkai area. *Miner. Depos.* **2002**, *21*, 264–269. (In Chinese with English Abstract)
51. Du, J.E.; Ma, C.H.; Zhang, G.H. Mineralization characteristics of the Changkeng gold-silver deposit, Guangdong province. *Guangdong Geol.* **1993**, *8*, 1–8. (In Chinese with English Abstract)
52. Wu, G.Y.; Liang, W.; Wei, L.; Li, X.Y. Geology feature and isotopic dating of Himalayan endogenetic mineralization in the Sanshui basin and its west margin, Guangdong Province. In *Study on Himalayan Endogenetic Mineralization*; Chen, Y., Wang, D., Eds.; Seismic Press: Beijing, China, 2001; pp. 117–129. (In Chinese)
53. Liu, B.; Shen, K. *Thermodynamics of Fluid Inclusions*; Geological Publishing House: Beijing, China, 1999. (In Chinese)
54. Lu, H.Z.; Fan, H.R.; Ni, P.; Ou, G.X.; Shen, K.; Zhang, W.H. *Fluid Inclusion*; Science Press: Beijing, China, 2004; pp. 1–487. (In Chinese)
55. Zhu, X.Q.; Wang, J.B.; Pang, Z.S.; Zhen, S.M.; Yang, F.; Xue, J.L.; Jia, H.X.; Shi, G.Y. Ore Geology, Fluid Inclusion Microthermometry and H-O-S Isotopes of the Liyuan Gold Deposit, Central Taihang Mountains, North China Craton. *Minerals* **2019**, *9*, 606. [[CrossRef](#)]
56. Zhang, P.; Kou, L.L.; Yan, Z.; Bi, Z.W.; Sha, D.M.; Li, Z.M.; Han, P.P. Fluid inclusions, H-O, S, Pb, and noble gas isotope studies of the Baiyun gold deposit in the Qingchengzi orefield, NE China. *J. Geochem. Explor.* **2019**, *200*, 37–53. [[CrossRef](#)]
57. Clayton, R.N.; Mayeda, T.K. The use of bromine pentafluoride in the extraction of oxygen from oxides and silicates for isotopic analysis. *Geochim. Cosmochim. Acta* **1963**, *27*, 43–52. [[CrossRef](#)]
58. Coleman, M.L.; Sheppard, T.J.; Durham, J.J.; Rouse, J.E.; Moore, G.R. Reduction of water with zinc for hydrogen isotope analysis. *Anal. Chem.* **1982**, *54*, 993–995. [[CrossRef](#)]
59. Li, C.; Love, G.D.; Lyons, T.W.; Fike, D.A.; Sessions, A.L.; Chu, X.L. A stratified redox model for the Ediacaran ocean. *Science* **2010**, *328*, 80–83. [[CrossRef](#)]
60. Friedman, I.; O'Neil, J.R. *Compilation of Stable Isotope Fractionation Factors of Geochemical Interest. Data of Geochemistry*; United States Government Printing Office: Washington, DC, USA, 1977; pp. 1–12.
61. Roedder, E. Fluid inclusions. *Rev. Miner.* **1984**, *12*, 644.
62. Walrafen, G.E. Raman spectral studies of water structure. *J. Chem. Phys.* **1964**, *40*, 3249–3256. [[CrossRef](#)]
63. Clayton, R.N.; O'Neil, J.R.; Mayeda, T.K. Oxygen isotope exchange between quartz and water. *J. Geophys. Res.* **1972**, *77*, 3057–3067. [[CrossRef](#)]
64. Xia, P.; Zhang, H.; Wang, X.Z.; Cheng, J.P. Geological and geochemical characteristics and genesis of the siliceous rocks in the Changkeng gold-silver district. *Geochemica* **1996**, *25*, 129–139. (In Chinese with English Abstract)

65. Guan, K.; Qiu, Y.S.; Yan, Z.Y. Geological characteristics and genesis of Changkeng gold deposit in Guangdong. *J. Precious Met. Geol.* **1997**, *6*, 27–37. (In Chinese with English Abstract)
66. Stuart, F.M.; Burnard, P.G.; Taylor, R.P.; Turner, G. Resolving mantle and crustal contributions to ancient hydrothermal fluids: He-Ar isotopes in fluid inclusions from Dae Hwa W-Mo mineralisation, South Korea. *Geochim. Cosmochim. Acta* **1995**, *59*, 4663–4673. [[CrossRef](#)]
67. Kendrick, M.A.; Burgess, R.; Patrick, R.A.D.; Turner, G. Fluid inclusion noble gas and halogen evidence on the origin of Cu-Porphyry mineralising fluids. *Geochim. Cosmochim. Acta* **2001**, *65*, 2651–2668. [[CrossRef](#)]
68. Chen, Y.J.; Chen, H.Y.; Zaw, K.; Pirajno, F.; Zhang, Z.J. Geodynamic settings and tectonic model of skarn gold deposit in China: An overview. *Ore Geol. Rev.* **2007**, *31*, 139–169. [[CrossRef](#)]
69. Liu, T.; Xiong, S.F.; Jiang, S.Y.; Li, H.L.; Chen, Q.Z.; Jiang, H. Genesis of the Zhijiadi Ag-Pb-Zn Deposit, Central North China Craton: Constraints from Fluid Inclusions and Stable Isotope Data. *Geofluids* **2017**, *2017*, 4153618. [[CrossRef](#)]
70. Taylor, H.P. The application of oxygen and hydrogen isotope studies to problems of hydrothermal alteration and ore deposition. *Econ. Geol.* **1974**, *69*, 843–883. [[CrossRef](#)]
71. Wilkinson, J.J. Fluid inclusions in hydrothermal ore deposit. *Lithos* **2001**, *55*, 229–272. [[CrossRef](#)]
72. Richards, J.P.; Bray, C.J.; Channer, D.D.; Spooner, E.T.C. Fluid chemistry and processes at the Porgera gold deposit, Papua New Guinea. *Miner. Depos.* **1997**, *32*, 119–132. [[CrossRef](#)]
73. Lotfia, F.; Belkabila, A.; Brunetb, S.; Brown, A.C.; Marcoux, E. Litho-geochemical, mineralogical analyses and oxygen-hydrogen isotopes of the Hercynian Koudiat Aicha massive sulphide deposit, Morocco. *J. Afr. Earth Sci.* **2010**, *56*, 150–166. [[CrossRef](#)]
74. Wagner, T.; Mlynarczyk, M.S.J.; Williams-Jones, A.E.; Boyce, A.J. Stable isotope constraints on ore formation at the San Rafael Tin-Copper Deposit, Southeast Peru. *Econ. Geol.* **2009**, *104*, 223–248. [[CrossRef](#)]
75. Qiu, K.F.; Yu, H.C.; Deng, J.; McIntire, D.; Gou, Z.Y.; Geng, J.Z.; Chang, Z.S.; Zhu, R.; Li, K.N.; Goldfarb, R.J. The giant Zaozigou orogenic Au-Sb deposit in West Qinling, China: Magmatic or metamorphic origin? *Miner. Depos.* **2020**, *55*, 345–362. [[CrossRef](#)]
76. Long, Z.Y.; Qiu, K.F.; Santosh, M.; Yu, H.C.; Jiang, X.Y.; Zou, L.Q.; Tang, D.W. Fingerprinting the metal source and cycling of the world's largest antimony deposit in Xikuangshan, China. *GSA Bull.* **2022**. [[CrossRef](#)]
77. Qiu, K.F.; Yu, H.C.; Hetherington, C.; Huang, Y.Q.; Yang, T.; Deng, J. Tourmaline composition and boron isotope signature as a tracer of magmatic-hydrothermal processes. *Mineralogis* **2021**, *106*, 1033–1044. [[CrossRef](#)]
78. Wang, L.Q.; Tang, J.X.; Cheng, W.B.; Chen, W.; Zhang, Z.; Lin, X.; Luo, M.C.; Yang, C. Origin of the ore-forming fluids and metals of the Bangpu porphyry Mo-Cu deposit of Tibet, China: Constraints from He-Ar, H-O, S and Pb isotopes. *J. Asian Earth Sci.* **2015**, *103*, 276–287. [[CrossRef](#)]
79. Simmons, S.F.; Sawkins, F.J.; Schlutter, D.J. Mantle-derived helium in two Peruvian hydrothermal ore deposit. *Nature* **1987**, *329*, 429–432. [[CrossRef](#)]
80. Burnard, P.G.; Hu, R.Z.; Turner, G.; Bi, X.W. Mantle, crustal and atmospheric noble gases in Ailaoshan gold deposit, Yunnan province, China. *Geochim. Cosmochim. Acta* **1999**, *63*, 1595–1604. [[CrossRef](#)]
81. Shen, J.F.; Santosh, M.; Li, S.R.; Li, C.P.; Zhang, J.Q.; Zhang, S.Q.; Alam, M.; Wang, Y.H.; Xu, K.X. He-Ar, S, Pb and O isotope geochemistry of the Dabaiyang gold deposit: Implications for the relationship between gold metallogeny and destruction of the North China Craton. *Ore Geol. Rev.* **2020**, *116*, 103229. [[CrossRef](#)]
82. Li, N.; Yang, F.Q.; Zhang, Z.X. Fluid inclusions and isotope (C, H, O, S, He, and Ar) study of the Xiaobaishitou skarn W-(Mo) deposit, East Tianshan, NW China. *Ore Geol. Rev.* **2020**, *122*, 103520. [[CrossRef](#)]
83. Yang, C.D.; Zhang, B.; Yang, F.Q.; Li, Q.; Wang, W.Q. Zircon u-pb age, fluid inclusion, and H-C-O-He-Ar-S isotopic compositions as an index to the VMS-type mineralization: A case study from the Wulasigou polymetallic deposit, Altay Orogenic Belt, Northwest China. *J. Geochem. Explor.* **2020**, *222*, 106720. [[CrossRef](#)]
84. Zeng, Q.D.; He, H.Y.; Zhu, R.X.; Zhang, S.; Wang, Y.B.; Su, F. Origin of ore-forming fluids of the Haigou gold deposit in the eastern Central Asian Orogenic belt, NE China: Constraints from H-O-He-Ar isotopes. *J. Asian Earth Sci.* **2017**, *144*, 384–397. [[CrossRef](#)]
85. Mamyin, B.A.; Tolstikhin, I.N. *Helium Isotopes in Nature*; Elsevier Pnb. Company: Amsterdam, The Netherlands, 1984; p. 273.
86. Ohmoto, H. Stable isotope geochemistry of ore deposits. *Rev. Miner. Geochem.* **1986**, *16*, 491–559.
87. Branam, T.D.; Ripley, E.M. Genesis of sediment-hosted copper mineralization in south-central Kansas: Sulfur/carbon and sulfur isotope systematics. *Econ. Geol.* **1990**, *85*, 601–621. [[CrossRef](#)]
88. Du, L.J.; Li, B.; Huang, Z.L.; Zhou, J.X.; Zou, G.F.; Yan, Z.F. Carbon-oxygen isotopic geochemistry of the Yangla Cu skarn deposit, SW China: Implications for the source and evolution of hydrothermal fluids. *Ore Geol. Rev.* **2017**, *88*, 809–821. [[CrossRef](#)]
89. Deines, P. Stable isotope variations in carbonatites. In *Carbonatites: Genesis and Evolution*; Bell, K., Ed.; Unwin Hyman: London, UK, 1989; pp. 301–359.
90. Veizer, J.; Hoefs, J. The nature of  $^{18}\text{O}/^{16}\text{O}$  and  $^{13}\text{C}/^{12}\text{C}$  secular trends in sedimentary carbonate rocks. *Geochim. Cosmochim. Acta* **1976**, *40*, 1387–1395. [[CrossRef](#)]
91. Zheng, Y.F.; Hoefs, J. Carbon and oxygen isotopic covariations in hydrothermal calcites. *Miner. Depos.* **1993**, *28*, 79–89. [[CrossRef](#)]
92. Liu, J.J.; Zheng, M.H.; Cook, N.J.; Long, X.R.; Deng, J.; Zhai, Y.S. Geological and geochemical characteristics of the Sawaya'erdun gold deposit, southwestern Chinese Tianshan. *Ore Geol. Rev.* **2007**, *32*, 125–156. [[CrossRef](#)]
93. Xue, Y.; Campbell, I.; Ireland, T.R.; Holden, P.; Armstrong, R. No mass-independent S isotope fractionation in auriferous fluids supports a magmatic origin for Archean gold deposit. *Geology* **2013**, *41*, 791–794. [[CrossRef](#)]
94. Selvaraja, V.; Caruso, S.; Fiorentini, M.L.; LaFlamme, C.; Bui, T.H. Atmospheric sulfur in the orogenic gold deposit of the Archaean Yilgarn Craton. *Geology* **2017**, *45*, 691–694.

95. Liang, J.L.; Li, J.; Sun, W.D.; Zhao, J.; Zhai, W.; Huang, Y.; Song, M.C.; Ni, S.J.; Xiang, Q.R.; Zhang, J.C.; et al. Source of ore-forming fluids of the Yangshan gold field, western Qinling orogen, China: Evidence from microthermometry, noble gas isotopes and in situ sulfur isotopes of Au-carrying pyrite. *Ore Geol. Rev.* **2019**, *105*, 404–422. [[CrossRef](#)]
96. Xu, R.; Li, W.C.; Deng, M.G.; Zhou, J.X.; Ren, T.; Yu, H.J. Genesis of the superlarge Luziyuan Zn-Pb-Fe(-Cu) distal skarn deposit in western Yunnan (SW China): Insights from ore geology and C-H-O-S isotopes. *Ore Geol. Rev.* **2019**, *104*, 944–959. [[CrossRef](#)]
97. Qiu, K.F.; Taylor, R.D.; Song, Y.H.; Yu, H.C.; Song, K.R.; Li, N. Geologic and geochemical insights into the formation of the Taiyangshan porphyry copper-molybdenum deposit, western Qinling orogenic belt, China. *Gondwana Res.* **2016**, *35*, 40–58. [[CrossRef](#)]
98. Qiu, K.F.; Marsh, E.; Yu, H.C.; Pfaff, K.; Gulbransen, C.; Gou, Z.Y.; Li, N. Fluid and metal sources of the Wenquan porphyry molybdenum deposit, Western Qinling, NW China. *Ore Geol. Rev.* **2017**, *86*, 459–473. [[CrossRef](#)]
99. Kesler, S.E.; Riciputi, L.C.; Ye, Z. Evidence for a magmatic origin for Carlin-type gold deposits: Isotopic composition of sulfur in the Betze-Post-Screamer Deposit, Nevada, USA. *Miner. Depos.* **2005**, *40*, 127–136. [[CrossRef](#)]
100. Chang, Z.; Large, R.R.; Maslennikov, V. Sulfur isotopes in sediment-hosted orogenic gold deposits: Evidence for an early timing and a seawater sulfur source. *Geology* **2008**, *36*, 971–974. [[CrossRef](#)]
101. Ma, J.; Lü, X.; Escolme, A.; Li, S.; Zhao, N.; Cao, X.; Zhang, L.J.; Lu, F. In-situ sulfur isotope analysis of pyrite from the Pangjiahe gold deposit: Implications for variable sulfur sources in the north and south gold belt of the South Qinling orogen. *Ore Geol. Rev.* **2018**, *98*, 38–61. [[CrossRef](#)]
102. Ohmoto, H.; Rye, R. Isotopes of sulfur and carbon. In *Geochemistry of Hydrothermal Ore Deposits*; Barnes, H.L., Ed.; John Wiley & Sons Inc.: New York, NY, USA, 1979; pp. 509–567.
103. Rye, R.O. The evolution of magmatic fluids in the epithermal environment: The stable isotope perspective. *Econ. Geol.* **1993**, *88*, 733–752. [[CrossRef](#)]
104. Kouhestani, H.; Ghaderi, M.; Chang, Z.; Zaw, K. Constraints on the ore fluids in the Chah Zard breccia-hosted epithermal Au–Ag deposit, Iran: Fluid inclusions and stable isotope studies. *Ore Geol. Rev.* **2015**, *65*, 512–521. [[CrossRef](#)]
105. Yilmaz, H.; Oyman, T.; Arehart, G.B.; Colakoglu, A.R.; Billor, Z. Low-sulfidation type Au–Ag mineralization at Bergama, Izmir, Turkey. *Ore Geol. Rev.* **2007**, *32*, 81–124. [[CrossRef](#)]
106. Yuan, M.W.; Li, S.R.; Li, C.L.; Santosh, M.; Alam, M.; Zeng, Y.J. Geochemical and isotopic composition of auriferous pyrite from the Yongxin gold deposit, Central Asian Orogenic Belt: Implication for ore genesis. *Ore Geol. Rev.* **2018**, *93*, 255–267. [[CrossRef](#)]
107. Yang, L.; Wang, Q.; Large, R.R.; Mukherjee, I.; Deng, J.; Li, H.; Yu, H.; Wang, X. Fluid source and metal precipitation mechanism of sediment-hosted Chang’an orogenic gold deposit, SW China: Constraints from sulfide texture, trace element, S, Pb, and He–Ar isotopes and calcite C–O isotopes. *Am. Mineral.* **2021**, *106*, 410–429. [[CrossRef](#)]
108. Wang, Z.; Zhang, X.; Liu, Q.; Shao, Y.; Wu, S.; Pan, Z.; Chen, M.; Zhang, Y.; Wu, H. Genesis of the Lishupo gold deposit in the Jiangnan Orogen, NE Hunan (South China): Biotite Ar–Ar, zircon U–Pb ages and H–O–S–Pb isotopic constraints. *Ore Geol. Rev.* **2022**, *145*, 104890. [[CrossRef](#)]
109. Zhu, B.Q. *Theory and Application of Isotope System in Geoscience*; Science Press: Beijing, China, 1998; p. 224. (In Chinese)
110. Wei, R.; Wang, Y.T.; Mao, J.W.; Hu, Q.J.; Qin, S.T.; Liu, S.Y.; Ye, D.J.; Yuan, Q.H.; Dou, P. Genesis of the Changba–Lijiagou Giant Pb–Zn Deposit, West Qinling, Central China: Constraints from S–Pb–C–O isotopes. *Acta Geol. Sin.* **2020**, *94*, 884–900. [[CrossRef](#)]
111. Zartman, R.E.; Doe, B.R. Plumbotectonics—The model. *Tectonophysics* **1981**, *75*, 135–162. [[CrossRef](#)]
112. Xue, J.L.; Pang, Z.S.; Ye, T.Z.; Zhen, S.M.; Tao, W.; Yang, T.T. Study of metallogenic regularity and prospecting prediction of gold deposit in China. *Earth Sci. Front.* **2017**, *24*, 1–14. (In Chinese with English Abstract)
113. Ye, T.Z.; Lv, Z.C.; Pang, Z.S. *Theory and Method of Prospecting Prediction in Exploration Area (General Introduction)*; Geological Publishing House: Beijing, China, 2014; pp. 362–404. (In Chinese)
114. Zhang, D.H. *Geochemistry of Ore-Forming Processes*; Geological Publishing House: Beijing, China, 2015; pp. 85–100. (In Chinese)
115. Wang, D.H.; Chen, Y.C.; Li, J.W.; Wei, L.; Li, X.Y.; Li, C.J. Ore-forming epoch of Hengjiang Pb–Zn–Cu deposit on western margin of Sanshui basin, Guangdong province, and its significance in prospecting for Cenozoic copper deposit. *Miner. Depos.* **2006**, *25*, 10–16. (In Chinese with English Abstract)
116. Railsback, L.B. An Earth scientist’s periodic table of the element and their ions. *Geology* **2003**, *31*, 737–740. [[CrossRef](#)]
117. Barnes, H.L. “Solubilities of Ore Minerals” in *Geochemistry of Hydrothermal Ore Deposits*; Wiley: New York, NY, USA, 1979; pp. 404–460.
118. Brimhall, G.H.; Crerar, D.A. Ore fluids: Magmatic to supergene. *Rev. Mineral. Geochem.* **1987**, *17*, 235–321.
119. Li, T.G.; Wu, G.; Liu, J.; Wang, G.R.; Hu, Y.Q.; Zahng, Y.F.; Luo, D.F.; Mao, Z.H.; Xu, B. Geochronology, fluid inclusions and isotopic characteristics of the Chaganbulagen Pb–Zn–Ag deposit, Inner Mongolia, China. *Lithos* **2016**, *261*, 340–355. [[CrossRef](#)]
120. Einaudi, M.T.; Hedenquist, J.W.; Inan, E.E. Chapter 15: Sulfidation state of fluids in active and extinct hydrothermal systems: Transitions from porphyry to epithermal environments. In *Special Publication of Society of Economic Geologists, No. 10: Volcanic, Geothermal, and Ore-Forming Fluids: Rulers and Witnesses of Processes within the Earth*; Simmons, S.F., Graham, I., Eds.; Society of Economic Geologists: Littleton, CO, USA, 2003; pp. 285–313.
121. Sillitoe, R.H.; Hedenquist, J.W. Chapter 16: Linkages between volcanotectonic settings, ore-fluid compositions, and epithermal precious metal deposit. In *Special Publication of Society of Economic Geologists, No. 10: Volcanic, Geothermal, and Ore-Forming Fluids: Rulers and Witnesses of Processes within the Earth*; Simmons, S.F., Graham, I., Eds.; Society of Economic Geologists: Littleton, CO, USA, 2003; pp. 315–343.

122. Rajabpour, S.; Jiang, S.Y.; Lehmann, B.; Abedini, A.; Gregory, D.D. Fluid inclusion and O-H-C isotopic, constraints on the origin and evolution of ore-forming fluids of the Cenozoic volcanic-hosted Kuh-Pang copper deposit, Central Iran. *Ore Geol. Rev.* **2018**, *94*, 277–289. [[CrossRef](#)]
123. Goldfarb, R.J.; Qiu, K.F.; Deng, J.; Chen, Y.J.; Yang, L.Q. Orogenic gold deposits of China. *SEG Spec. Publ.* **2019**, *22*, 263–324.
124. Cooke, D.R.; Simmons, S.F. Characteristics and genesis of epithermal gold deposits. *Rev. Econ. Geol.* **2000**, *13*, 221–244.
125. Simmons, S.F.; White, N.C.; John, D.A. Geological characteristics of epithermal precious and base metal deposits. In *Economic Geology 100th Anniversary Volume*; Hedenquist, J.W., Thompson, J.F.H., Goldfarb, R.J., Richards, J.P., Eds.; Society of Economic Geologists: Littleton, CO, USA, 2005; pp. 485–522.